Editors' Suggestion

Benchmark calculations of pure neutron matter with realistic nucleon-nucleon interactions

M. Piarulli,[1] I. Bombaci,[2,3] D. Logoteta,[2,3] A. Lovato,[4,5] and R. B. Wiringa[4]
[1]*Physics Department, Washington University, St Louis, Missouri 63130, USA*
[2]*Dipartimento di Fisica "E. Fermi", Università di Pisa, Largo B. Pontecorvo 3, I-56127 Pisa, Italy*
[3]*INFN, Sezione di Pisa, Largo B. Pontecorvo 3, I-56127 Pisa, Italy*
[4]*Physics Division, Argonne National Laboratory, Argonne, Illinois 60439, USA*
[5]*INFN-TIFPA Trento Institute of Fundamental Physics and Applications, 38123 Trento, Italy*

(Received 19 August 2019; revised manuscript received 9 December 2019; accepted 24 February 2020; published 8 April 2020)

We report benchmark calculations of the energy per particle of pure neutron matter as a function of the baryon density using three independent many-body methods: Brueckner–Bethe–Goldstone, Fermi hypernetted chain/single-operator chain, and auxiliary-field diffusion Monte Carlo. Significant technical improvements are implemented in the latter two methods. The calculations are made for two distinct families of realistic coordinate-space nucleon-nucleon potentials fit to scattering data, including the standard Argonne v_{18} interaction and two of its simplified versions, and four of the new Norfolk Δ-full chiral effective field theory potentials. Primarily because of the advancements in the auxiliary-field diffusion Monte Carlo, we observe good agreement among the three many-body techniques up to nuclear saturation density—the maximum difference in the energy per particle is within 1.5 MeV for all the potentials we consider. At higher densities, the divergences become more important, and are mainly driven by the Fermi hypernetted chain/single-operator calculations. We also study the connection between nucleon-nucleon scattering data and the energy per particle of pure neutron matter. Our results suggest that fitting to higher-energy nucleon-nucleon scattering helps reduce the spread of energies among the models.

DOI: 10.1103/PhysRevC.101.045801

I. INTRODUCTION

The quest for understanding static and dynamic properties of nuclear systems in terms of nucleon-nucleon (NN) and three-nucleon ($3N$) forces, and consistent electroweak currents has long been considered one of the most challenging efforts of nuclear theory. Over the past 20 years, establishing this microscopic approach to nuclear physics has undergone substantial progress, driven by two major factors. First, since the advent of chiral effective field theory (χEFT), originally proposed by Weinberg in the early 1990s [1,2], we can now systematically develop nuclear many-body interactions [3–6] and consistent electroweak currents [7–13] that are rooted in the fundamental symmetries exhibited by the underlying theory of quantum chromodynamics. Second, present computational resources allow us to employ these interactions and currents in sophisticated many-body methods to compute a variety of nuclear systems with controlled approximations [14–20]. The chief challenge for this microscopic approach is to accurately describe atomic nuclei—including their spectra, form factors, transitions, low-energy scattering, and response—while simultaneously predicting properties of infinite matter, e.g., pure neutron matter (PNM), relevant to the structure and internal composition of neutron stars.

The past few years have marked the birth of the multimessenger astronomy era [21], which has opened new windows to probe the constituents of matter and their interactions under extreme conditions that cannot be reproduced in terrestrial laboratories. The first direct detection of gravitational-waves from coalescing neutron stars by the LIGO-Virgo interferometer network [22,23], followed by a short burst of γ rays and later optical and infrared signals–the event GW170817 [21,24]—effectively constrains their masses, spins and tidal deformability [25–27]. In addition, the multiple measurements of two-solar masses neutron stars [28–32] are posing intriguing questions about how dense matter can support such large masses against gravitational collapse.

The equation of state (EoS) of strongly interacting matter is a thermodynamic relation between the energy (pressure), the baryon density, and the temperature. While the description of core-collapse supernovae and the formation and cooling of proton-neutron stars requires the finite-temperature EoS, already a few minutes after its birth, neutron star properties can be safely described using the EoS of cold (zero temperature) neutron-rich matter [33]. In the region between the inner crust and the outer core ($\sim 0.5 - 2\rho_0$, with $\rho_0 = 0.16$ fm^{-3} being the nuclear saturation density), neutron stars are mainly composed of neutrons, in β equilibrium with a small fraction of protons, electrons and muons. Different scenarios have been suggested to model the high-density regime, from nucleon degrees of freedom only but with many-nucleon forces and relativistic effects [34–44], to including the formation of heavier baryons containing strange quarks [45–49], to quark matter [50–53], or other more exotic condensates [54–56].

While the determination of the maximum mass of a neutron star requires knowing the EoS up to several times nuclear saturation density, it is the region up to $\sim 2\rho_0$ that effectively controls their radii. In this density regime, the PNM EoS can play an important role for testing the microscopic model Hamiltonians fit to *NN* scattering data and few-body observables against astrophysical constraints. However, microscopic calculations of the EoS with reliable error estimates up to $2\rho_0$ provide useful insights on how measurements of the tidal polarizabilities from binary neutron-star mergers can unravel properties of matter at supranuclear densities [26].

In addition to the uncertainties arising from modeling the nuclear Hamiltonian, which can in principle be assessed by testing the order-by-order convergence of the chiral expansion [57], microscopic calculations of the EoS are also affected by the approximations inherent to the method used for solving the many-body Schrödinger equation. To gauge them, we perform benchmark calculations of the energy per particle of pure neutron matter as a function of the baryon density using three independent many-body methods: the Brueckner–Bethe–Goldstone (BBG) [15,58], the Fermi hypernetted chain/single-operator chain (FHNC/SOC) [59,60], and the auxiliary-field diffusion Monte Carlo (AFDMC) [61]. In our analysis, we consider the widely used Argonne v_{18} (AV18) *NN* potential [62]—and its simplified versions AV8′ and AV6′ [63]—and the recently derived Norfolk NV2 χEFT *NN* forces [64,65], which explicitly include the Δ isobar intermediate state. While the BBG method is not limited to interactions that are local in coordinate space, the latter are simpler to treat in continuum quantum Monte Carlo (QMC) methods because the two-body propagator is essentially positive definite [66]. FHNC/SOC is also ideally suited to deal with local potentials, as nonlocalities introduce high-order derivatives that are nontrivial to account for in the hypernetted chain equations.

The scope of this work is not to achieve a realistic description of the EoS of PNM, which would require the inclusion of many-nucleon forces, as for instance in Refs. [34–36,43,44]. We are rather mostly interested in quantitatively assessing the systematic error of the different many-body approaches and how this error depends upon the nuclear interaction of choice. The authors of Ref. [67] argued that the discrepancies among the methods are particularly susceptible to the spin-orbit components of the *NN* force. To identify and reduce these differences, we implement two major advancements in the AFDMC algorithm, both in the sampling procedure and in the way the fermion sign problem is controlled, in a similar fashion as recently done for atomic nuclei [68,69]. The FHNC/SOC approach is also made more accurate by including classes of elementary diagrams that have been disregarded in earlier applications of the method. As compared to the FHNC/SOC results reported in Ref. [67], here we also include spin-orbit correlations, which turns out to be the numerically more important difference.

Recently, the scale dependence of both AV18 and the local χEFT interactions of Refs. [70,71] has been investigated analyzing their predictions for *NN* scattering data and deuteron properties [72]. The main conclusion of that work is that phenomenological potentials appear to be best suited to study the high-density region of the EoS. Here, we extend this analysis comparing the energy per particle of PNM as obtained from both the Argonne and Norfolk *NN* interactions, relating their predictive power in describing the EoS at $\rho > \rho_0$ to their capability of reproducing *NN* scattering data as a function of the laboratory energy.

The plan of this paper is as follows. The Argonne and Norfolk Hamiltonians are described in Sec. II, where we also show the phase shifts predicted by the various *NN* potentials. The many-body methods employed for calculating the EoS of PNM are reviewed in Sec. III, along with a detailed discussions of their technical improvements. The results obtained within the BBG, FHNC/SOC, and AFDMC approaches for the different Hamiltonians are benchmarked in Sec. IV. Finally, in Sec. V we summarize our findings and draw our conclusions.

II. NUCLEAR INTERACTIONS

In recent years local, configuration-space chiral interactions, well suited for use in QMC calculations of light-nuclei spectra and neutron-matter properties, have been derived by two groups [43,70,71,73–76]. In this paper, we will base our calculations on high-quality local potentials derived from a χEFT that explicitly includes—in addition to nucleons and virtual pions—virtual Δ's as degrees of freedom [64,65,76,77]. The two-nucleon part (*NN*) of such local interactions is written as the sum of an electromagnetic interaction component, $v_{ij}^{\rm EM}$, (as in Ref. [62]), and a strong-interaction component, v_{ij}, characterized by long- and short-range parts [65], respectively, $v_{ij}^{\rm L}$ and $v_{ij}^{\rm S}$. The $v_{ij}^{\rm L}$ part includes one-pion-exchange (OPE) and two-pion-exchange (TPE) terms up to next-to-next-to-leading order (N2LO) in the chiral expansion [64], derived in the static limit from leading and subleading πN and $\pi N\Delta$ chiral Lagrangians. The radial functions involved in the definition of $v_{ij}^{\rm L}$ are explicitly given in Appendix A of Ref. [64]. They are singular at the origin (they behave as $1/r_{ij}^n$ with $r_{ij} = |\mathbf{r}_i - \mathbf{r}_j|$ and n taking on values up to $n = 6$), and each is regularized by a cutoff of the form

$$C_{R_{\rm L}}(r_{ij}) = 1 - \frac{1}{(r_{ij}/R_{\rm L})^6\, e^{(r_{ij}-R_{\rm L})/a_{\rm L}} + 1}, \tag{1}$$

where three values for the radius $R_{\rm L} = (0.8, 1.0, 1.2)$ fm are considered with the diffuseness fixed at $a_{\rm L} = R_{\rm L}/2$ in each case.

The $v_{12}^{\rm S}$ part, however, is described by contact terms up to next-to-next-to-next-to-leading order (N3LO) [65], characterized by 26 low-energy constants (LECs). These interactions have been recently constrained to a large set of *NN*-scattering data, as assembled by the Granada group [78], including the deuteron ground-state energy and two-neutron scattering length. The radial functions entering the $v_{12}^{\rm S}$ component are the same as those listed in Appendix B of Ref. [64], and involve a local regulator (to replace the δ functions) taken as

$$C_{R_{\rm S}}(r_{ij}) = \frac{1}{\pi^{3/2} R_{\rm S}^3} e^{-(r_{ij}/R_{\rm S})^2}, \tag{2}$$

where we consider, in combination with $R_L = (0.8, 1.0, 1.2)$ fm, $R_S = (0.6, 0.7, 0.8)$ fm, corresponding to typical momentum-space cutoffs $\Lambda_S = 2\hbar c/R_S$ ranging from about 660 MeV down to 500 MeV.

We constructed two classes of *NN* interactions, which only differ in the range of laboratory energy over which the fits were carried out, either 0–125 MeV in class I or 0–200 MeV in class II. For each class, three different sets of cutoff radii (R_S, R_L) were considered $(R_S, R_L) = (0.8, 1.2)$ fm in set a, (0.7,1.0) fm in set b, and (0.6,0.8) fm in set c. We are referring to these high-quality *NN* interactions generically as the Norfolk (NV2) potentials, and denote those in class I as NV2-Ia, NV2-Ib, and NV2-Ic, and those in class II as NV2-IIa, NV2-IIb, and NV2-IIc.

For the purpose of this paper, we will focus our attention on calculations of the EoS of neutron matter involving the NV2 local chiral *NN* interactions described above and leave the inclusion of the corresponding three-nucleon force [13,76,77] to future study. Comparison will be made with the phenomenological AV18 potential [62]. Both the Argonne and Norfolk interactions are defined in coordinate space as

$$v_{ij} = \sum_{p=1}^{N} v^p(r_{ij}) O_{ij}^p, \tag{3}$$

with $r_{ij} = |\mathbf{r}_i - \mathbf{r}_j|$. For the Argonne potential $N = 18$—hence the name Argonne v_{18} or AV18—while the NV2 potentials have $N = 16$. The bulk of the *NN* interaction is encoded in the first eight operators

$$O_{ij}^{p=1-8} = [1, \sigma_{ij}, S_{ij}, \mathbf{L}\cdot\mathbf{S}] \otimes [1, \tau_{ij}], \tag{4}$$

which are the same for both AV18 and the NV2s. In the above equation we introduced $\sigma_{ij} = \boldsymbol{\sigma}_i \cdot \boldsymbol{\sigma}_j$ and $\tau_{ij} = \boldsymbol{\tau}_i \cdot \boldsymbol{\tau}_j$ with $\boldsymbol{\sigma}_i$ and $\boldsymbol{\tau}_i$ being the Pauli matrices acting in the spin and isospin space. The tensor operator is given by

$$S_{ij} = \frac{3}{r_{ij}^2}(\boldsymbol{\sigma}_i \cdot \mathbf{r}_{ij})(\boldsymbol{\sigma}_j \cdot \mathbf{r}_{ij}) - \sigma_{ij}, \tag{5}$$

while the spin-orbit contribution is expressed in terms of the relative angular momentum $\mathbf{L} = \frac{1}{2i}(\mathbf{r}_i - \mathbf{r}_j) \times (\boldsymbol{\nabla}_i - \boldsymbol{\nabla}_j)$ and the total spin $\mathbf{S} = \frac{1}{2}(\boldsymbol{\sigma}_i + \boldsymbol{\sigma}_j)$ of the pair. For AV18 there are six additional charge-independent operators corresponding to $p = 9 - 14$ that are quadratic in $\mathbf{L}$, while the $p = 15 - 18$ are charge-independence breaking terms. In contrast, the NV2 potentials have three charge-independent operators quadratic in $\mathbf{L}$, and five charge-independence breaking terms.

It is useful to define simpler versions of the AV18 and NV2 potentials with fewer operators: a v_8' with the eight operators of Eq. (4) and a v_6' without the $\mathbf{L}\cdot\mathbf{S} \otimes [1, \tau_{ij}]$ terms [63,79]. The v_8' is a reprojection (rather than a simple truncation) of the strong-interaction potential that reproduces the charge-independent average of $^1S_0$, $^3S_1$-$^3D_1$, $^1P_1$, $^3P_0$, $^3P_1$, and (almost) $^3P_2$ phase shifts by construction, while overbinding the deuteron by 18 keV due to the omission of electromagnetic terms. The v_6' is (mostly) a truncation of v_8' which reproduces $^1S_0$ and $^1P_1$ partial waves, makes a slight adjustment to (almost) match the v_8' deuteron and $^3S_1$-$^3D_1$ partial waves, but will no longer split the ^3P_J partial waves properly. We will refer to these variations of the Argonne potential as AV8′ and AV6′.

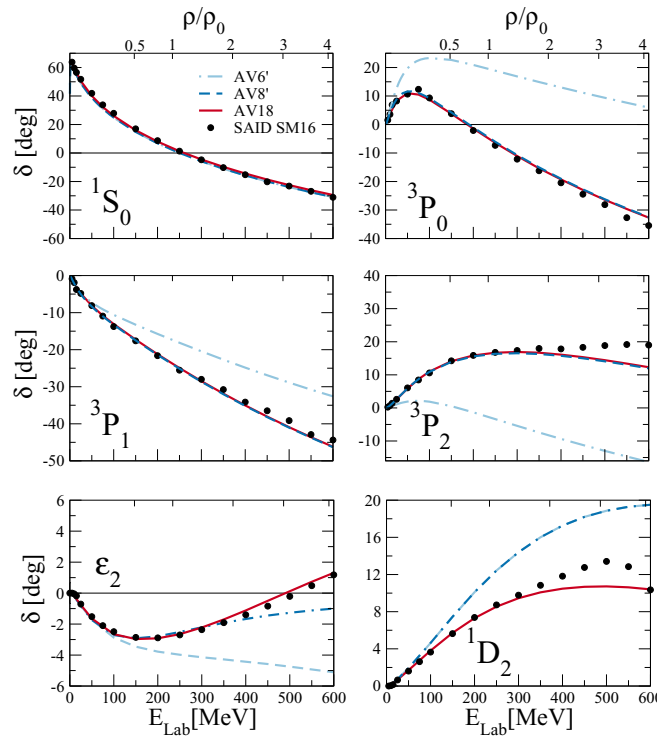

FIG. 1. Neutron-proton scattering phase shifts in the $^1S_0$, $^3P_0$, $^3P_1$, and $^3P_2$, ϵ_2, and $^1D_2$ channels, as a function of kinetic energy of the beam particle in the laboratory frame (bottom axis). The corresponding densities of PNM—in units of ρ_0—are given in the top axis. The long-dashed-dotted, the dashed- and the solid lines represent the AV6′, AV8′, and AV18 predictions, while the solid dots are from the SM16 solution of Ref. [80].

In strongly degenerate systems of fermions, such as the low-temperature nucleonic matter forming the interior of neutron stars, collisions primarily involve nucleons occupying states close to the Fermi surface. As a consequence, in the case of head-on scattering, a relation can be easily established between the kinetic energy of the beam particle in the laboratory frame, $E_{\rm lab}$, and the Fermi energy E_F, which in turn is simply related to the baryon density ρ. The resulting expression in PNM is

$$E_{\rm lab} = 2E_{\rm cm} = 4E_F = \frac{2\hbar^2}{m}(3\pi^2\rho)^{2/3}. \tag{6}$$

In Ref. [72] the above expression has been utilized to gauge the predictive power of *NN* potential models in describing the high-density regime of PNM. Along the same line, Fig. 1 illustrates the energy dependence of the proton-neutron scattering phase shifts in the $^1S_0$, $^3P_0$, $^3P_1$, $^3P_2$, ϵ_2, and $^1D_2$ partial waves comparing the AV6′, AV8′, and AV18 potentials with the analysis of Ref. [80]. In Fig. 2 we show the predictions for the same quantities obtained from the set of NV2 Δ-full local χEFT interactions discussed above. The density of PNM obtained from Eq. (6) with $E_{\rm lab} = 2E_{\rm cm}$ is reported on the top axis of the figures in units of the nuclear saturation density

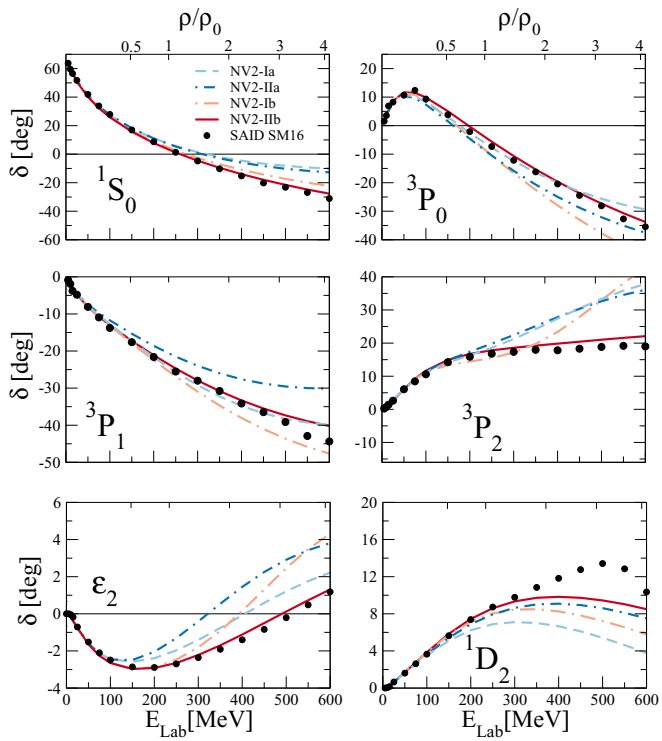

FIG. 2. Same as Fig. 1, but for the NV2 Δ-full local χEFT interactions. The dashed- and short-dashed-dotted lines represent the predictions for the NV2-Ia and NV2-IIa models, having $R_S = 0.8$ fm and, respectively, constrained to *NN*-scattering data up to 125 and 200 MeV laboratory energy. The long-dashed-dotted and the solid lines show results for the NV2-Ib and NV2-IIb models, having $R_S = 0.7$ fm and, respectively, constrained to *NN*-scattering data up to 125 and 200 MeV laboratory energy. The solid dots are from the SM16 solution of Ref. [80].

$\rho_0 = 0.16$ fm^{-3}. The AV18 interaction provides an accurate description of the scattering data up to $E_{\rm lab} \simeq 600$ MeV and appears to be applicable to describe properties of PNM at least up to $\rho \simeq 4\rho_0$. The greatest discrepancy appears in the ^{1}D$_2$ channel, where inelasticity becomes important at higher energy.

As opposed to the AV18 potential, χEFT models, which are based on low momentum expansion, are intrinsically limited in describing dense systems, in which *NN* interactions involve high energies. In addition, chiral potentials depend on regulator function that smoothly cuts off one- and two-pion exchange interactions at short distances, and the choice of such cutoff, here defined as R_S, plays a crucial role in describing short-range dynamics. In Fig. 2, we notice that the chiral model NV2-IIb, which is fitted at higher energies ($E_{\rm lab} =$ 200 MeV) with a hard cutoff (∼600 MeV in momentum-space) achieves a better description of the *S*- and *P*- phase shifts up to ∼600 MeV. Such a model performs very like the AV18, which has been fitted up to the pion production threshold ($E_{\rm lab} = 350$ MeV) with a very hard cutoff (∼1 GeV).

It has to be noted that the ability of reproducing *NN* scattering data at relatively large $E_{\rm lab} \simeq 600$ has to be considered a necessary, rather than sufficient, condition to accurately describe neutron matter properties at supranuclear densities. It is always possible to perform a unitary transformation of the two-body potential that leaves the phase-shifts unchanged [81]. In general, the transformed interaction would behave very differently from the bare one in the infinite medium, and one needs to account for the induced many-body interactions to recover the original results.

III. MANY-BODY METHODS

In this section we review the many-body methods employed for calculating the EoS of PNM and provide a detailed discussions of their technical improvements. In all approaches the two-body interaction v_{ij} is the only physical input for the numerical calculations. We note that while AFDMC and FHNC/SOC techniques are limited to semi-local interactions, the BBG method can also treat potentials not formulated in coordinate space.

A. Brueckner–Bethe–Goldstone many-body theory

The Brueckner–Bethe–Goldstone many-body theory (see, e.g., Refs. [15,58]) is based on a linked cluster expansion (the so-called hole-line expansion) of the energy per nucleon E/A of nuclear matter. The various terms of the expansion can be represented by Goldstone diagrams [82] grouped according to the number of independent hole-lines (i.e., lines representing empty single particle states in the Fermi sea). The basic ingredient in this approach is the Brueckner reaction matrix G [83,84] which sums, in a closed form, the infinite series of the so-called ladder diagrams and allows treatment of the short-range strongly repulsive part of the nucleon-nucleon interaction. The G-matrix can be obtained by solving the Bethe–Goldstone equation [85]

$$G(\omega) = V + V \sum_{k_a,k_b} \frac{|\mathbf{k_a},\mathbf{k_b}\rangle\, Q\, \langle \mathbf{k_a},\mathbf{k_b}|}{\omega - \epsilon(k_a) - \epsilon(k_b) + i\eta}\, G(\omega), \qquad (7)$$

where V is the bare *NN* interaction, ϵ is the single-particle energy, and the quantity ω is the so-called starting energy. In the present work we consider spin-unpolarized neutron matter, thus in Eq. (7) and in the following equations we drop the spin indices to simplify the mathematical notation. The Pauli operator $|\mathbf{k_a},\mathbf{k_b}\rangle Q \langle \mathbf{k_a},\mathbf{k_b}|$ projects on intermediate scattering states in which the momenta $\mathbf{k_a}$ and $\mathbf{k_b}$ of the two interacting neutrons are above their Fermi momentum k_F because single particle states with momenta smaller than this value are occupied by the neutrons of the nuclear medium. Thus the Bethe–Goldstone equation describes the scattering of two nucleons (two neutrons in our case) in the presence of other nucleons, and the Brueckner G-matrix represents the effective interaction between two nucleons in the nuclear medium and properly takes into account the short-range correlations arising from the strongly repulsive core in the bare *NN* interaction.

The $\epsilon(k)$ of a neutron with momentum $\mathbf{k}$, appearing in the energy denominator of the Bethe–Goldstone Eq. (7), is given

by

$$\epsilon(k) = \frac{\hbar^2 k^2}{2m} + U(k), \tag{8}$$

where $U(k)$ is a single-particle potential which represents the mean field felt by a neutron due to its interaction with the other neutrons of the medium. In the Brueckner–Hartree–Fock (BHF) approximation of the BBG theory, $U(k)$ is calculated through the real part of the G-matrix [86,87] and is given by

$$U(k) = \sum_{k' \leqslant k_F} \mathrm{Re}\langle \mathbf{k}, \mathbf{k}' | G(\omega^*) | \mathbf{k}, \mathbf{k}' \rangle_A, \tag{9}$$

where the sum runs over all neutron occupied states, the starting energy is $\omega = \omega^* \equiv \epsilon(k) + \epsilon(k')$ (i.e., the G-matrix is calculated on-the-energy-shell) and the matrix elements are properly antisymmetrized. We make use of the so-called continuous choice [88–91] for the single-particle potential $U(k)$ when solving the Bethe–Goldstone equation. As it has been shown in Refs. [92–94], the contribution of the three-hole-line diagrams to the energy per nucleon E/A is minimized in this prescription for the single-particle potential and a faster convergence of the hole-line expansion for E/A is achieved compared to the so-called gap choice for $U(k)$.

In this scheme Eqs. (7)–(9) have to be solved self-consistently using an iterative numerical procedure. Once a self-consistent solution is achieved, the energy per nucleon of the system can be evaluated in the BHF approximation of the BBG hole line-expansion and it is given by

$$\frac{E}{A} = \frac{1}{A} \sum_{k<k_F} \left[\frac{\hbar^2 k^2}{2m} + \frac{1}{2} U(k) \right]. \tag{10}$$

Making the usual angular average of the Pauli operator and of the energy denominator [89,91], the Bethe–Goldstone Eq. (7) can be expanded in partial waves. In all the calculations performed in this work, we have considered partial wave contributions up to a total two-body angular momentum $J_{\max} = 11$. We have verified that the inclusion of partial waves with $J_{\max} > 11$ does not appreciably change our results.

B. Fermi hypernetted chain/single-operator chain method

In absence of interactions, a uniform system of A noninteracting neutrons can be described as a Fermi gas at zero temperature, and its ground state wave function reduces to the Slater determinant of orbitals associated with the single-particle states belonging to the Fermi sea

$$\Phi(X) = \mathcal{A}\big[\phi_{n_1}(x_1) \ldots \phi_{n_A}(x_A)\big]. \tag{11}$$

In the above equation $X = \{x_1, \ldots, x_A\}$, where the generalized coordinate $x_i \equiv \{\mathbf{r}_i, s_i\}$ represents both the position $R = \mathbf{r}_1, \ldots, \mathbf{r}_A$ and the spin $S = s_1, \ldots, s_A$, variables of the ith nucleon while n_i denotes the set of quantum numbers specifying the single particle state. Translational invariance imposes that the single-particle wave functions be plane waves,

$$\phi_{n_i}(x_i) = \frac{1}{\sqrt{\Omega}} e^{i\mathbf{k}_i \cdot \mathbf{r}_i} \chi_{\sigma_i}(s_i). \tag{12}$$

In the above equations, Ω is the normalization volume, $\chi_{\sigma_i}(s_i)$ is the spinor of the neutron and $|\mathbf{k}_i| < k_F = (3\pi^2\rho)^{1/3}$. Here k_F is the Fermi momentum and ρ the density of the system.

The variational ansatz of the Fermi hypernetted chain (FHNC) and single-operator chain (SOC) formalism emerges as a generalization of the Jastrow theory of Fermi liquids [60,95]

$$|\Psi_T\rangle = \frac{F|\Phi\rangle}{\langle \Phi | F^\dagger F | \Phi \rangle^{1/2}}, \tag{13}$$

where $|\Phi\rangle$ is the Slater determinant of Eq. (11) and

$$F(x_1, \ldots, x_A) = \mathcal{S}\left(\prod_{j>i=1}^{A} F_{ij} \right) \tag{14}$$

is the correlation operator. The spin-isospin structure of F_{ij} reflects that of the nucleon-nucleon potential of Eq. (3),

$$F_{ij} = \sum_{p=1}^{8} f^p(r_{ij}) O_{ij}^p. \tag{15}$$

Since, in general, $[O_{ij}^p, O_{ik}^q] \neq 0$, the symmetrization operator $\mathcal{S}$ is needed to fulfill the requirement of antisymmetrization of the wave-function. The $f^p(r_{ij})$ are finite-ranged functions, with the conditions

$$\begin{aligned} f^p(r \geqslant d_p) &= \delta_{p1}, \\ \left. \frac{df^p(r)}{dr} \right|_{r=d_p} &= 0, \end{aligned} \tag{16}$$

where the d_p are "healing distances." Consequently, the correlation operator of Eq. (14) respects the cluster property: If the system is split in two (or more) subsets of particles that are moved far away from each other, then the F factorizes into a product of two factors in such a way that only particles belonging to the same subset are correlated. For instance, consider two subsets, say $i_1, \ldots i_M$ and $i_{M+1}, \ldots i_A$. The cluster property implies

$$F(x_1, \ldots, x_A) = F\left(x_{i_1}, \ldots, x_{i_M}\right) F\left(x_{i_{M+1}}, \ldots, x_A\right). \tag{17}$$

The radial functions $f^p(r_{ij})$ are determined by minimizing the energy expectation value

$$E_V = \langle \Psi_T | H | \Psi_T \rangle \geqslant E_0, \tag{18}$$

which provides an upper bound to the true ground state energy E_0. The cluster property allows one to expand the expectation value of the Hamiltonian—and of other many-body operators—between correlated states in a sum of cluster contributions involving an increasing number of particles.

The energy expectation value in matter is evaluated using a diagrammatic cluster expansion and a set of 29 coupled integral equations, which effectively make partial summations to infinite order—the FHNC/SOC approximation [60]. This is a generalization of the original hypernetted chain (HNC) method for Bose systems developed by van Leeuwen, Groeneveld, and de Boer [96], which requires the solution of a single integral equation, and the corresponding extension for spin-isospin independent Fermi systems by Fantoni and Rosati [59], which requires four coupled integral equations.

The integral equations are used to generate two- and three-body distribution functions $g_2(r_{ij}) \equiv g_{ij}$ and $g_3(\mathbf{r}_{ij}, \mathbf{r}_{ik}) \equiv g_{ijk}$, which can then be used to evaluate the energy or other operators.

For the pure Jastrow case, we evaluate the Pandharipande–Bethe [97] expression for the energy:

$$E_{\rm PB} = T_F + W + W_F + U + U_F, \tag{19}$$

where T_F is the Fermi gas kinetic energy. The only terms for a Bose system are

$$W = \frac{\rho}{2}\int \left(v_{ij} - \frac{\hbar^2}{m}\frac{\nabla^2 F_{ij}}{F_{ij}}\right) g_{ij} d^3 r_{ij},$$
$$U = -\frac{\hbar^2}{2m}\frac{\rho^2}{4}\int \left(\frac{\boldsymbol{\nabla}_i F_{ij}\cdot\boldsymbol{\nabla}_i F_{ik}}{F_{ij}F_{ik}}\right) g_{ijk} d^3 r_{ij} d^3 r_{ik}, \tag{20}$$

while W_F, U_F are additional two- and three-body kinetic energy terms present due to the Slater determinant. Alternately, we use the Jackson–Feenberg [98] energy expression

$$E_{\rm JF} = T_F + W_B + W_\phi + U_\phi, \tag{21}$$
$$W_B = \frac{\rho}{2}\int \left[v_{ij} - \frac{\hbar^2}{2m}\left(\frac{\nabla^2 f_{ij}}{f_{ij}} - \frac{(\nabla_i f_{ij})^2}{f_{ij}^2}\right)\right], \tag{22}$$

where W_B is the boson term and W_ϕ and U_ϕ are kinetic energy terms involving the Slater determinant. In principle, these energies should be equivalent, but in practice there are differences due to the FHNC/SOC approximation to the distribution functions. We take the average $E_V = (E_{\rm PB} + E_{\rm JF})/2$ as our energy expectation value and the difference $\delta E_V = |E_{\rm PB} - E_{\rm JF}|/2$ as an estimate of the error in the calculation.

The FHNC two-body distribution function can be written as

$$g_{ij} = f^2[(1 + G_{de} + \mathcal{E}_{de})^2 + G_{ee} + \mathcal{E}_{ee} - \nu(G_{cc} + \mathcal{E}_{cc} - \ell/\nu)^2]\exp(G_{dd} + \mathcal{E}_{dd}), \tag{23}$$

where the chain functions G_{xy} are sums of nodal diagrams, with direct (d), exchange (e), or circular exchange (c) end points, $\mathcal{E}_{xy}$ are elementary diagrams, $\ell \equiv \ell(k_F r)$ is the Slater function, and ν is the degeneracy. An example of the structure of the integral equations is

$$G_{dd,ij} = \rho\int d^3 r_k [(X_{dd,ik} + X_{de,ik})S_{dd,kj} + X_{dd,ij} S_{de,kj}], \tag{24}$$

where $S_{dd} = f^2\exp(G_{dd} + \mathcal{E}_{dd}) - 1$ is a two-point superbond and $X_{dd} = S_{dd} - G_{dd}$ is a link function.

The introduction of spin-isospin correlations with operators that do not commute complicates the calculation. Fortunately, the first six operators $p = 1, 6$ form a closed spin-isospin algebra, allowing single continuous chains of operator links—the SOCs—to be evaluated. These involve five chain functions G^p_{xy} for each of the five operators $p = 2$–6, with $xy = dd, de, ee, ca, cb$ in addition to the four Jastow chain functions in Eq. (23), making the total of 29 coupled integral equations to be solved. There are significant contributions from unlinked diagrams in the SOC cluster expansion, but these can be accommodated by means of "vertex" corrections, as discussed in Ref. [60]. Additional higher-order corrections coming from (parallel) multiple operator chains and rings are also calculated, as discussed in Ref. [35].

As opposed to the FHNC/SOC calculations reported in Ref. [67], in this work we include spin-orbit correlations, corresponding to the $p = 7, 8$ terms in Eq. (15). Because of the presence of a derivative operator, these correlations cannot be "chained" so they are treated explicitly only at the two- and three-body cluster level. It has to be noted that while the two-body cluster contribution is evaluated exactly, following the prescription of Ref. [35] only a limited number of three-body terms in the cluster expansion are kept.

In standard FHNC calculations, the elementary diagrams of Eq. (23) are generally neglected. Inclusion of the leading four-body elementary diagram leads to the FHNC/4 approximation [99], while additional contributions have been studied in liquid atomic helium systems [100]. In the present work we include many central ($p = 1$) $\mathcal{E}_{xy}$ diagrams, beyond the FHNC/4 approximation, by introducing three-point superbonds S_{xyz}, such as

$$S_{ddd,123} = \rho\int d^3 r_4 \{S_{dd,14}S_{dd,24}(S_{dd,34} + S_{de,34}) + (S_{dd,14}S_{de,24} + S_{de,14}S_{dd,24})S_{dd,34}\}, \tag{25}$$

and then evaluating

$$\mathcal{E}_{dd,12} = \frac{1}{2}\rho\int d^3 r_3 \{S_{ddd,132}[S_{dd,13}(S_{dd,32} + S_{de,32}) + S_{de,13}S_{dd,32}] + S_{ded,132}S_{dd,24}S_{dd,32}\}. \tag{26}$$

With six S_{xyz}, where $xyz = ddd, dde, dee, eee, ccd$, and cce, many elementary diagrams at the four-, five-, and higher-body level contributing to g_{ij} and g_{ijk} can be evaluated. These central elementary diagrams also dress the SOCs.

In matter calculations, the correlations of Eq. (16) are generated by solving a set of coupled Euler-Lagrange equations in different pair-spin and isospin channels for $S = 0, 1$ and $T = 0, 1$. For pure neutron matter, only $T = 1$ channels are needed, leaving a single-channel equation for $S = 0$, producing a singlet correlation, and a triple-channel equation for $S = 1$, which produces triplet, tensor, and spin-orbit correlations. The singlet and triplet correlations are then projected into central and σ_{ij} combinations. Three (increasing) healing distances are used: d_s for the singlet correlation, d_p for the triplet and spin-orbit, and d_t for the tensor.

Additional variational parameters are the quenching factors α_p whose introduction simulates modifications of the two–body potentials entering in the Euler–Lagrange differential equations arising from the screening induced by the presence of the nuclear medium

$$v_{ij} = \sum_{p=1}^{8} \alpha_p v^p(r_{ij}) O^p_{ij}, \tag{27}$$

whereas the full potential is used when computing the energy expectation value. In practice we use just two such parameters: $\alpha_{p=1} = 1$ and $\alpha_{p=2,8} = \alpha$. In addition, the resulting

correlation functions f^p may be rescaled according to

$$F_{ij} = \sum_{p=1}^{8} \beta_p f^p(r_{ij}) O^p_{ij}, \tag{28}$$

with $\beta_{p=1} = 1$, $\beta_{p=2,4+7,8} = \beta_\sigma$, and $\beta_{p=5,6} = \beta_t$. However, these are usually invoked only in the presence of three-body forces. For the present work, the variational parameters are the three healing distances and one quenching factor. These are varied at each density with a simplex search routine to minimize the energy.

One measure of the convergence of the FHNC/SOC integral equations is that the volume integral of the correlation hole from the central part of the two-body distribution function g_{ij} [which has operator components like the F_{ij} of Eq. (15)] should be unity. To help guarantee that the variational parameters entering the FHNC/SOC correlations are well behaved—and to ensure that in a given region of the parameter space the cluster expansion is converged—we minimize the energy plus a constant times the deviation of the volume integral from unity:

$$E + C\left\{1 + \rho \int d^3r[g^c(r) - 1]\right\}^2,$$

as discussed in Ref. [35]. A value of $C = 1000$ MeV is sufficient to limit the violation of this sum rule to 1% or less at normal density, and 3% or less at twice normal density for all the potentials considered here. There is a related sum rule for the isospin component g^τ that applies in symmetric nuclear matter, but there is no sum rule for the spin correlation hole for realistic potentials with tensor forces.

C. Auxiliary-field diffusion Monte Carlo

Over the past two decades, the auxiliary-field diffusion Monte Carlo (AFDMC) method [61] has become a mainstay for neutron-matter calculations [43,74,101]. Within AFDMC, properties of the infinite uniform system are simulated with a finite number of neutrons obeying the periodic-box boundary condition (PBC). The trial wave function is a simplified version of the one reported in Eq. (13),

$$\Psi_T(X) = \langle X|\Psi_T\rangle = \langle X|\left(\prod_{i<j} f^c(r_{ij})\right)|\Phi\rangle. \tag{29}$$

The antisymmetric mean-field part $|\Phi\rangle$ is the Slater determinant of Eq. (11). To satisfy the PBC, the single-particle wave vector is discretized as

$$\mathbf{k}_i = \frac{2\pi}{L}\{n_x, n_y, n_z\}, \quad n_i = 0, \pm1, \pm2, \ldots, \tag{30}$$

L being the size of the simulation box. When not otherwise specified, in our simulations we typically employ $A = 66$ neutrons in a box. Finite-size errors in PNM simulations have been investigated in Ref. [102,103] by comparing the twist averaged boundary conditions with the PBC. Remarkably, the PBC energies of 66 neutrons differ by no more than 2% from the asymptotic value calculated with twist averaged boundary conditions. This essentially follows from the fact that the kinetic energy of 66 fermions approaches the thermodynamic limit very well. Additional finite-size effects due to the tail corrections of two- and three-body potentials are accounted for by summing the contributions given by neighboring cells to the simulation box [104].

The spin-independent correlation ansatz of Eq. (29) has proven to be inadequate to treat atomic nuclei and infinite nucleonic matter composed of both neutrons and protons. In fact, the expectation value of the tensor components of the *NN* potential, which is large for neutron-proton pairs in the $T = 0$ channel, is nearly zero when tensor correlations are not included in $\Psi_T(X)$. To overcome these difficulties, a linearized version of spin-dependent two-body correlations, in which only one pair of nucleons is correlated at a time, was first implemented in the AFDMC method in Ref. [68]. Very recently, the trial wave function has been further improved by including quadratic pair correlations [69]. These more sophisticated wave functions have enabled a number of remarkably accurate AFDMC calculations, in which properties of atomic nuclei with up to $A = 16$ nucleons [105] have been investigated utilizing the local χEFT interactions of Ref. [43,70].

Analogously to the FHNC case, the two-body correlation functions are obtained by minimizing the two-body cluster contributions of the energy per particle, solving the same set of coupled Euler-Lagrange equations. However, since in Ψ_T we only retain spin-independent terms, we found that replacing $f^c(r_{ij}) \to f^c(r_{ij}) + \beta_\sigma f^\sigma(r_{ij})$, β_σ being a variational parameter, provides a better variational energy than when $\beta_\sigma = 0$. The relatively simple trial wave function of Eq. (29) is completely determined by three variational parameters: β_σ, the spin-isospin potential quencher $\alpha_{p=2,8} = \alpha$, and the central healing distance d_c, as for simplicity we assume $d_s = d_p = d_c$. As a consequence, it is unnecessary to use advanced optimization algorithms, such as the "stochastic reconfiguration" [106] or the "linear method" [107] algorithm, to minimize the variational energy.

AFDMC is an extension of standard diffusion Monte Carlo (DMC) algorithms, in which the ground-state Ψ_0 of a given Hamiltonian is projected out from the starting trial wave function using an imaginary-time evolution,

$$|\Psi_0\rangle = \lim_{\tau\to\infty} e^{-(H-E_T)\tau}|\Psi_T\rangle. \tag{31}$$

In the above equation τ is the imaginary time, and E_T is a parameter used to control the normalization. For strongly interacting systems, the direct computation of the propagator $e^{-(H-E_0)\tau}$ involves prohibitive difficulties. For small imaginary times $\delta\tau = \tau/N$, with N being a large number, one can compute the short-time propagator, and the full propagation can be recovered inserting complete sets of states. The propagated wave function then reads

$$\langle X_N|\Psi(\tau)\rangle = \prod_{i=1}^{N-1}\int dX_i \langle X_N|e^{-(H-E_0)\delta\tau}|X_{N-1}\rangle \ldots \langle X_2|e^{-(H-E_0)\delta\tau}|X_1\rangle\langle X_1|\Psi_T\rangle. \tag{32}$$

By using the Suzuki-Trotter decomposition to order $\delta\tau^3$, the short-time propagator can be cast in the form

$$G(X, X', \delta\tau) = \langle X|e^{-(H-E_0)\delta\tau}|X'\rangle \simeq \langle X|e^{-V\frac{\delta\tau}{2}}e^{-T\delta\tau}e^{-V\frac{\delta\tau}{2}}|X'\rangle. \quad (33)$$

In the above equation, V is the nuclear potential and T is the nonrelativistic kinetic energy, giving rise to the free propagator

$$G_0(X, X', \delta\tau) = \langle X|e^{-T\delta\tau}|X'\rangle = \left(\frac{m}{2\pi\delta\tau}\right)^{\frac{3A}{2}} e^{-\frac{m(R-R')^2}{2\delta\tau}}\delta(S-S'), \quad (34)$$

where R and S denote the spatial and spin coordinates, respectively. Monte Carlo techniques are used to sample the paths X_i. In practice, a set of configurations, typically called *walkers,* are simultaneously evolved in imaginary time, and then used to calculate observables once convergence is reached.

Within the Green's function Monte Carlo (GFMC) method used in light nuclei, the positions of the particles are sampled, but the full sum over the spin-isospin degrees of of freedom is retained, leading to an exponential growth of the computational cost with A. The AFDMC method overcomes this limitation using a spin-isospin basis given by the outer product of single-nucleon spinors,

$$|S\rangle = |s_1\rangle \otimes |s_2\rangle \cdots \otimes |s_A\rangle. \quad (35)$$

Realistic nuclear potentials, such the ones employed in this work, contain quadratic spin-isospin operators. To preserve the single-particle representation, the short-time propagator is linearized utilizing the Hubbard-Stratonovich transformation,

$$e^{-\lambda O^2\delta\tau/2} = \frac{1}{\sqrt{2\pi}}\int_{-\infty}^{\infty} dx e^{-x^2/2}e^{x\sqrt{-\lambda\delta\tau}\,O}, \quad (36)$$

where x are the *auxiliary fields* and the operators O are obtained as follows. The first six terms defining the *NN* potential of Eq. (3) can be conveniently separated in a spin-isospin dependent $V_{\rm SD}$ and spin-isospin independent $V_{\rm SI}$ contributions. Since in purely neutron systems $\tau_{ij} = 1$, $V_{\rm SD}$ can be cast in the form

$$V_{\rm SD} = \frac{1}{2}\sum_{i\alpha j\beta} A_{i\alpha,j\beta}\sigma_i^\alpha\sigma_j^\beta = \frac{1}{2}\sum_{n=1}^{3A} O_n^2\lambda_n, \quad (37)$$

where the operators O_n are defined as

$$O_n = \sum_{i,\alpha}\sigma_i^\alpha\psi_{i\alpha}^n. \quad (38)$$

In the above equations λ_n and $\psi_{i\alpha}^n$ are the eigenvalues and eigenvectors of the matrix A. The spin-orbit term of the *NN* potentials is implemented in the propagator as described in Ref. [104] and appropriate counter terms are included to remove the spurious contributions of order $\delta\tau$.

Importance sampling techniques are routinely implemented in the AFDMC—in both the spatial coordinates and spin-isospin configurations—to drastically improve the efficiency of the algorithm. To this aim, the propagator of Eq. (33) is modified as

$$G_I(X, X') = G_I(X, X')\frac{\Psi_I(X')}{\Psi_I(X)}. \quad (39)$$

At each time-step, each walker is propagated sampling a $3A$-dimensional vector to shift the spatial coordinates and a set of auxiliary fields $\mathcal{X}$ from Gaussian distributions. To remove the linear terms coming from the exponential of Eqs. (34) and (36), in analogy to the GFMC method, we consider four weights, corresponding to separately flipping the sign of the spatial moves and spin-isospin rotations

$$w_i = \frac{\Psi_I[\pm R', S'(\pm\mathcal{X})]}{\Psi_I(R, S)}. \quad (40)$$

In the same spirit as the GFMC, only one of the four configurations is kept according to a heat-bath sampling among the four normalized weights w_i/W, with $W = \sum_{i=1}^4 w_i/4$ being the cumulative weight. The latter is then rescaled by $W \to W\exp[-V_{\rm SI}(R)/2 + V_{\rm SI}(R')/2 - E_T]\delta\tau\}$ and associated to this new configuration for branching and computing observables. This "plus and minus" procedure, introduced in Ref. [68] and so far only applied to systems including protons, is adopted in this work to compute the energy of PNM, as it significantly reduces the dependence of the results on $\delta\tau$.

The expectation values of observables that commute with the Hamiltonian are estimated as

$$\langle O(\tau)\rangle = \frac{\sum_X O_T(X)W_T(X)}{\sum_X W_T(X)}, \quad (41)$$

where

$$O_T(X) = \frac{\langle\Psi_T|O|X\rangle}{\langle\Psi_T|X\rangle}, \quad W_T(X) = W(X)\frac{\langle\Psi_T|X\rangle}{\langle\Psi_I|X\rangle}. \quad (42)$$

For all other observables we compute the mixed estimates

$$\langle O(\tau)\rangle \simeq 2\frac{\langle\Psi_T|O|\Psi(\tau)\rangle}{\langle\Psi_T|\Psi(\tau)\rangle} - \frac{\langle\Psi_T|O|\Psi_T\rangle}{\langle\Psi_T|\Psi_T\rangle}, \quad (43)$$

where the first and the second term correspond to the DMC and variational Monte Carlo expectation value, respectively.

As in standard fermion diffusion Monte Carlo algorithms, the AFDMC method suffers from the fermion sign problem. This originates from the fact that the importance-sampling wave-function is not exact and entails spuriosities from the bosonic ground-state of the system. As a consequence, the numerator and denominator of Eq. (41) are plagued by a decreasing signal-to-noise ratio for a finite sample size and large imaginary times. To alleviate the sign problem, as in Ref. [108], we implement an algorithm similar to the constrained-path approximation [109], but applicable to complex wave functions and propagators. The weights w_i of Eq. (40) are evaluated with

$$\frac{\Psi_I(R', S')}{\Psi_I(R, S)} \to {\rm Re}\left\{\frac{\Psi_T(R', S')}{\Psi_T(R, S)}\right\}. \quad (44)$$

and they are set to zero if the ratio is negative. Unlike the fixed-node approximation, which is applicable for scalar potentials and for cases in which a real wave function can be used, the solution obtained from the constrained propagation

is not the a rigorous upper-bound to the true ground-state energy [110]. To remove the bias associated with this procedure, the configurations obtained from a constrained propagation are further evolved using the following positive-definite importance sampling function [69,111]:

$$\Psi_G(X) = \sqrt{\mathrm{Re}\{\Psi_T(X)\}^2 + \alpha\,\mathrm{Im}\{\Psi_T(X)\}^2}, \qquad (45)$$

where the α parameter serves to make the guiding function positive definite. Throughout this work we take $\alpha = 0.5$ and we explicitly checked for selected cases that our result are unchanged for $\alpha = 0.25$ and $\alpha = 1$.

Following the unconstrained propagation, the expectation value of the energy $E_{\mathrm{UC}}(\tau)$ is estimated according to Eq. (41). The only difference, needed to compensate for the change of the guiding wave function, is that the weights need to be rescaled as

$$W(X) \to W(X)\frac{\Psi_G(X_0)}{\Psi_T(X_0)}, \qquad (46)$$

where X_0 is the initial configuration of the unconstrained propagation at $\tau = \tau_0$. In a typical calculation, ∼400 independent unconstrained propagations, each composed of an average of ∼140, 000 configurations, are performed to control statistical fluctuations. The asymptotic value $E_0 = \lim_{\tau\to\infty} E_{\mathrm{UC}}(\tau)$ is found by fitting the imaginary-time behavior of $E_{\mathrm{UC}}(\tau)$ with a single-exponential function, as in Ref. [79]. Since the expectation values are substantially correlated in τ, the likelihood function is computed by fully taking into account the covariance matrix of the data. We have explicitly checked that the number of independent unconstrained propagations is large enough to avoid potential instabilities arising when the covariance matrix has at least one very small eigenvalue [112]. The confidence interval associated with E_0 is estimated as discussed in Sec. 15.6 of Ref. [113]. The best value of the fit is perturbed in such a way that $\Delta\chi^2 = 1$ from its minimum while varying the other fitting parameters to minimize the χ^2. Since this procedure brings about an asymmetric confidence interval, in our results we report a symmetric error bar conservatively corresponding to the largest interval.

Unconstrained propagations have been performed in the latest AFDMC studies of atomic nuclei [69,105,114], even though a relatively simpler fitting procedure was employed to determine the asymptotic E_0 and its error. However, the accuracy of the constrained approximation for neutron systems has been erroneously assumed, even in the state-of-the art AFDMC neutron-matter calculations with local chiral interactions [70,74,115]. Figure 3 indeed shows that for the AV6′ potential at $\rho = \rho_0$ releasing the constraint brings about tiny changes to the constrained results. The situation is drastically different for *NN* potentials that include spin-orbit terms. The unconstrained propagation for the AV8′ potential at $\rho = 0.16$ fm^{-3} is displayed in Fig. 4—note the scale difference with Fig. 3. For this potential, $E_{\mathrm{UC}}(\tau)$ exhibits a clear exponentially-decaying behavior, lowering the energy per particle by as much as ∼3 MeV. Nearby points in imaginary-time are strongly correlated. If one assumes that the covariance matrix is diagonal, this correlation is lost, and the fit is dominated by the first values of $E_{\mathrm{UC}}(\tau)$, as they have small errors. Once the covariance matrix is accounted for, the values of the unconstrained energy at large τ become relatively more important in the fit.

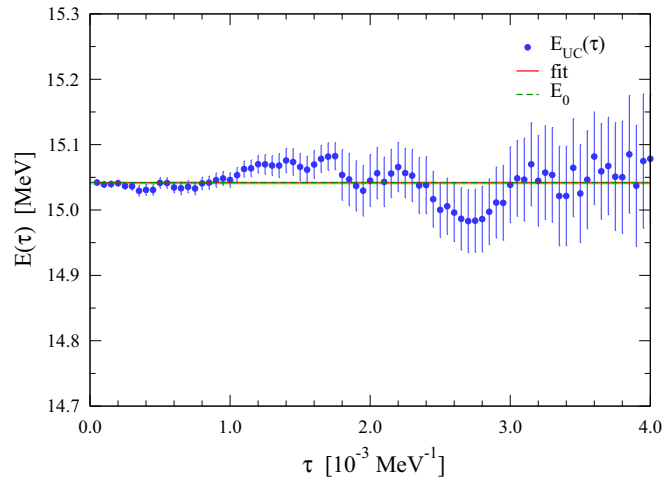

FIG. 3. PNM unconstrained evolution for the AV6′ potential at $\rho = 0.16$ fm^{-3} for 14 neutrons in PBC. Data points (in blue) refer to $E_{\mathrm{UC}}(\tau)$ while the dashed line and the shaded (green) area indicate the asymptotic value E_0 with the associated uncertainty as estimated from the fit, represented by the solid (red) line.

We checked that including linearized spin-dependent correlations in the trial wave function yields only ∼0.3 MeV of additional binding in the constrained propagation. Since their calculation increases the computational cost by a factor $\sim A^2$, we have decided not to include them as we need large statistics to reliably perform the imaginary-time extrapolation. However, the spin-dependent backflow correlations of Ref. [116] seems to be more effective: some preliminary calculations indicate that the constrained results can be lowered by more than ∼1 MeV per particle. However, given the complexity of the analytic calculation of the derivatives, particularly for the operators in the AV18 potential that are quadratic in **L**, we decided to stick to the simple central Jastrow ansatz of Eq. (29).

For both AV6′ and AV8′, we simulated PNM using 14 neutrons in PBC, correcting for the tails of the potential and

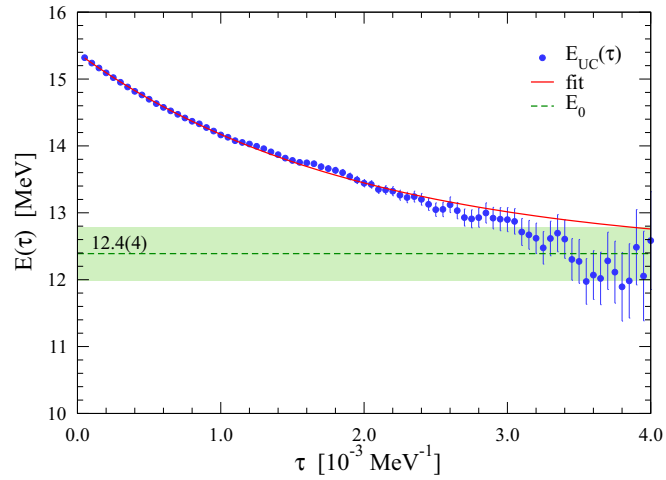

FIG. 4. Same as Fig. 4 for the AV8′ interaction.

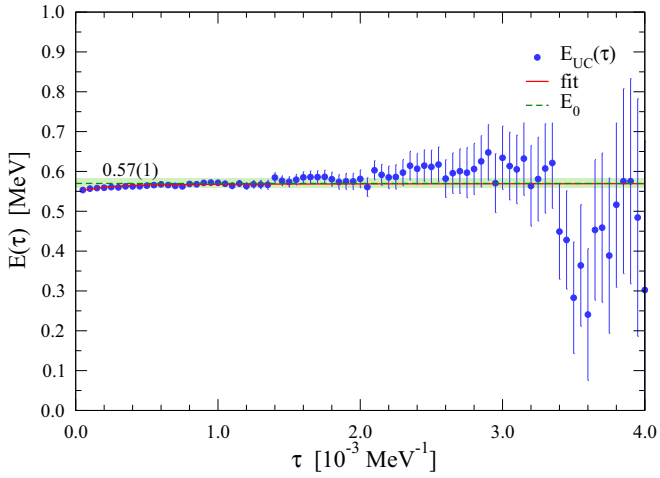

FIG. 5. PNM unconstrained evolution of $\langle v_{18} - v_8' \rangle$ for AV18 at $\rho = 0.16$ fm^{-3} for 14 neutrons in PBC. The notation is the same as in Fig. 4.

Jastrow correlations. The dependency on the box size of the AV8′ results has been tested by performing an additional calculation with 38 neutrons in a PBC. It turns out that $E_{\rm UC}(\tau) - E_{\rm UC}(\tau_0)$ obtained with the two simulation boxes are fully compatible within statistical errors. Our findings for the AV8′ interaction are consistent with the GFMC results of Ref. [117] and with the discrepancies in the spin-orbit splitting of neutron drops between AFDMC and GFMC calculations [111].

Analogously to the GFMC method, when computing the full AV18 and NV2 two-body interactions, the propagation is performed with the simplified v_8' potential, described in Sec. II. The expectation value $\langle v_{18} - v_8' \rangle$ is evaluated in perturbation theory according to Eq. (43). As shown in Fig. 5 for $\rho = 0.16$ and 14 neutrons with PBC, the potential energy difference remains fairly stable during the unconstrained propagation. We fit its imaginary time behavior with a simple inverse polynomial formula with up to $1/\tau^2$ powers and estimate the error on the asymptotic value accordingly.

IV. RESULTS

We compare the PNM equation of state as obtained from the three independent many-body methods described in Sec. III, using the Argonne and the Norfolk families of *NN* interactions. As for the AFDMC, we present results corresponding to both the constrained (AFDMC-CP) and unconstrained (AFDMC-UC) imaginary-time propagations. To minimize finite-size effects, AFDMC-CP calculations are carried out with 66 neutrons in a box with PBC. However, the unconstrained energy is estimated by adding to the AFDMC-CP values the energy difference $E_{\rm UC}(\tau) - E_{\rm UC}(\tau_0)$ computed simulating 14 neutrons with PBC. This procedure significantly reduces the computational cost of the calculation. Its accuracy is validated by the successful comparison of unconstrained propagations with 14 and 38 neutrons with PBC, discussed in the previous section.

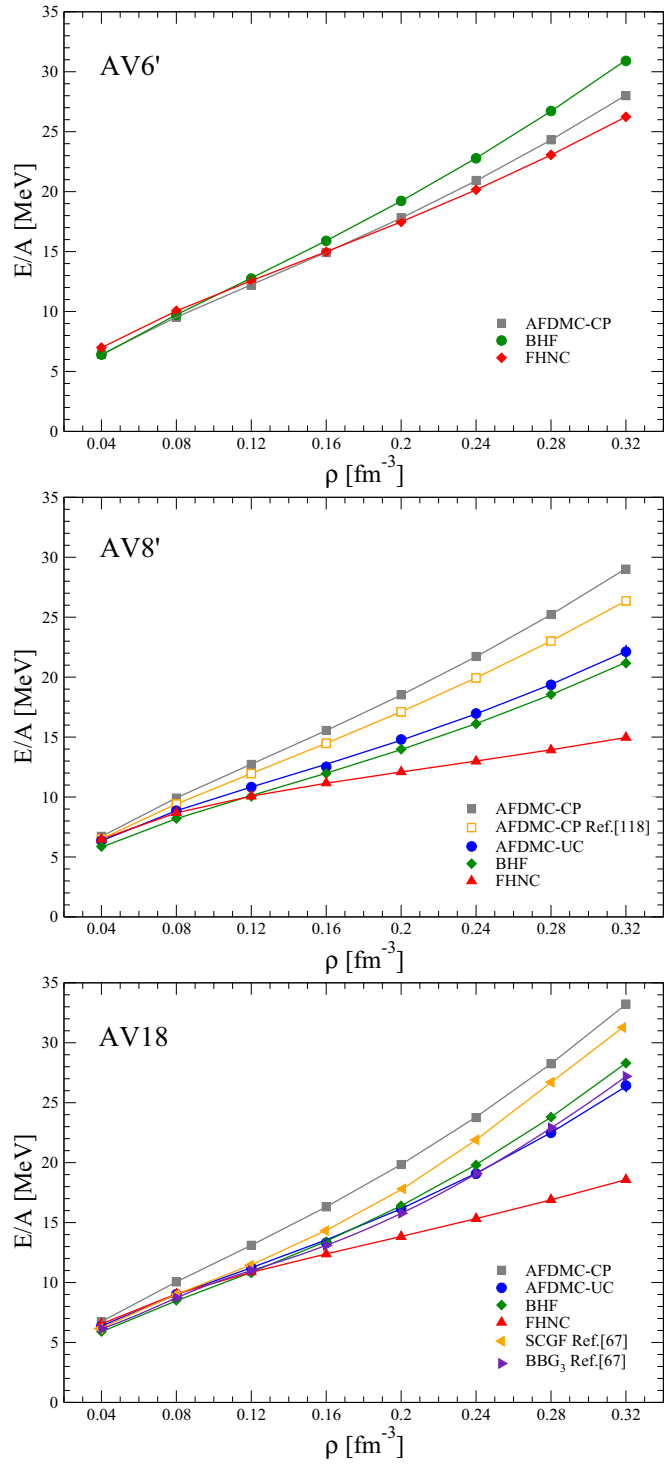

FIG. 6. Energy per particle of PNM as a function of density calculated with the BHF (green diamonds), FHNC/SOC (red triangles), AFDMC-CP (grey squares) and AFDMC-UC (solid blue points) many-body approaches. Results for the AV6′, AV8′, and AV18 potentials are shown in the upper, middle, and lower panels, respectively. The curves correspond to the polynomial fit of Eq. (47).

In the upper, middle, and lower panels of Fig. 6 we show the PNM equation of state for the AV6′, AV8′, and AV18 potentials, respectively. The curves in the plot correspond to

TABLE I. Total energy and spin-orbit potential per particle at nuclear saturation density for the AV6′, AV8′, and AV18 *NN* potentials as obtained from the BHF, FHNC/SOC, AFDMC-CP, and AFDMC-UC methods.

	BHF	FHNC/SOC	AFDMC-CP	AFDMC-UC
		E/A [MeV]		
AV6′	15.89	14.98 ± 0.22	14.93 ± 0.02	14.92 ± 0.05
AV8′	11.97	11.17 ± 0.19	15.55 ± 0.02	12.51 ± 0.39
AV18	13.40	12.38 ± 0.17	16.32 ± 0.02	13.32 ± 0.40
		$\langle v_{\rm LS}\rangle$ [MeV]		
AV8′	−9.50	−6.71	-0.65 ± 0.03	-5.4 ± 1.2
AV18	−7.93	−5.80	-0.55 ± 0.03	-5.2 ± 1.1

the following polynomial fit for the density dependence of the energy per particle

$$\frac{E(\rho)}{A} = a_{2/3}\left(\frac{\rho}{\rho_0}\right)^{2/3} + a_1\left(\frac{\rho}{\rho_0}\right) + a_2\left(\frac{\rho}{\rho_0}\right)^2, \qquad (47)$$

where $\rho = 0.16$ fm^{-3} is the nuclear saturation density. The first term corresponds to a free Fermi gas, while the second and third are inspired by the cluster expansion of the energy expectation value, truncated at the three-body level. We have checked that the four-parameter fitting function of Ref. [118] produces overlapping curves to the one obtained from Eq. (47).

To facilitate the comparison among the many-body methods, in Table I we list the energy per particle and the spin-orbit contribution at nuclear saturation density. As for the latter, since in neutron-matter $\tau_{ij} = 1$, we directly report the expectation value of sum of the $p = 7, 8$ operators of Eq. (4), denoted as $\langle v_{\rm LS}\rangle$. The FHNC/SOC method allows to directly access the expectation value of the spin-orbit terms of the potential. However, within both BHF and the AFDMC, $\langle v_{\rm LS}\rangle$ is obtained employing the Hellman-Feynman theorem. This amounts to computing the two ground-state energies $E_{\pm\epsilon} = \langle H \pm \epsilon\, v_{\rm LS}\rangle$, where ϵ is a small number. The spin-orbit contribution is estimated as

$$\langle v_{\rm LS}\rangle \simeq \frac{E_{+\epsilon} - E_{-\epsilon}}{2\epsilon}. \qquad (48)$$

Consistently with Ref. [67], when the AV6′ interaction is employed, the three many-body methods provide similar results for $E(\rho)/A$. Generally, BHF yields the most repulsive EoS, FHNC/SOC the softest, and the AFDMC-CP values are in between. Even at $\rho = 2\rho_0$, the maximum spread among the different methods remains within ∼5 MeV per particle. Note that the FHNC/SOC calculations shown in this work are more sophisticated than those of Ref. [67], as more elementary diagrams–at and beyond the FHNC/4 approximation—are accounted for. This leads to accurate estimates for the energy per particle, particularly when spin-orbit correlations are not included. The AFDMC-UC energies for AV6′ are not shown, as, within error bars, they overlap with the AFDMC-CP ones—see the unconstrained propagation of Fig. 3.

The inclusion of spin-orbit components of the AV8′ potential brings about an overall attraction in PNM with respect to the AV6′ results, for both BHF and FHNC/SOC methods. This appears to be a consequence of the isospin asymmetry: in GFMC calculations for light nuclei, AV6′ is more attractive for isospin-symmetric nuclei, but AV8′ is more attractive in neutron-rich systems [63]. For example, as seen in the associated force evolution table [119], the two models give the same energy for ^{6}He, while in ^{8}He, AV8′ is ≃1 MeV more bound. Also, the difference in binding between ^{8}Be and ^{8}He is 26.9 MeV for AV6′ and 24.2 MeV for AV8′, implying that AV8′ is bringing in relatively more attraction for the neutron-rich systems.

However, the AFDMC-CP energies per particle for AV8′ are slightly larger than those obtained with AV6′, and they lie well above both BHF and FHNC/SOC results, already at relatively small densities. As shown in Table I, at $\rho = \rho_0$, BHF, FHNC/SOC, and AFDMC-CP provide 11.97 MeV, 11.17 ± 0.19 MeV, and 15.55 ± 0.02 MeV per particle, respectively. The unconstrained propagation significantly lowers the AFDMC-CP estimates, bringing them in much better agreement with the other calculations. At $\rho = \rho_0$, the AFDMC-UC value turns out to be 12.51 ± 0.39 MeV, while at $\rho = 2\rho_0$ the unconstrained propagation yields 22.13 ± 0.52 MeV, to be compared to the 29.01 ± 0.01 MeV of the constrained approximation. The curve corresponding to the AFDMC-CP calculations of Ref. [118] lies below the AFDMC-CP obtained with the "plus and minus" importance-sampling algorithm. The differences between the two constrained approximations are largely due to the dependence on the central Jastrow correlations of the importance-sampling algorithm utilized in Ref. [118]. As noted in Ref. [70], for the local N2LO χEFT potential this unphysical dependence on the Jastrow function can be as large as 0.6 MeV per particle already at $\rho = 0.1$ fm^{-3}. Note that this dependence is completely removed once the "plus and minus" procedure is employed.

The FHNC/SOC results stay well below both the BHF and AFDMC-UC ones, with the spread increasing with the density. This behavior is most likely due to the oversimplified treatment of spin-orbit correlations, which becomes less accurate at higher densities, as contributions arising from clusters involving more than three nucleons should not be neglected. We explicitly checked that, as pointed out in Refs. [67,115,120], when the spin-obit correlations are turned off, FHNC/SOC and AFDMC-CP are in much better agreement. It is remarkable that the AFDMC-UC and BHF predictions are quite similar, the differences remaining well below 1 MeV per particle up to $\rho = 2\rho_0$. This corroborates the accuracy of the extrapolation of the unconstrained energy.

As in light nuclei, the AV18 potential, is more repulsive than AV8′ for all the many-body methods considered in this work. In particular, as the density increases, the differences in partial waves higher than P become more and more important. The AFDMC-CP results turn out to be biased to a similar extent as in the AV8′ case: the unconstrained propagation at $\rho = \rho_0$ and $\rho = 2\rho_0$ lowers the energy per particle by ∼3.0 MeV and ∼6.8 MeV, respectively. The BHF and AFDMC-UC predictions are again very close: the maximum difference remains below ∼1 MeV per particle. Contrary to the AV8′ case, AFDMC-UC yields slightly less repulsion than BHF. At $\rho > \rho_0$, the FHNC/SOC results lie significantly below those computed within both AFDMC-UC and BHF.

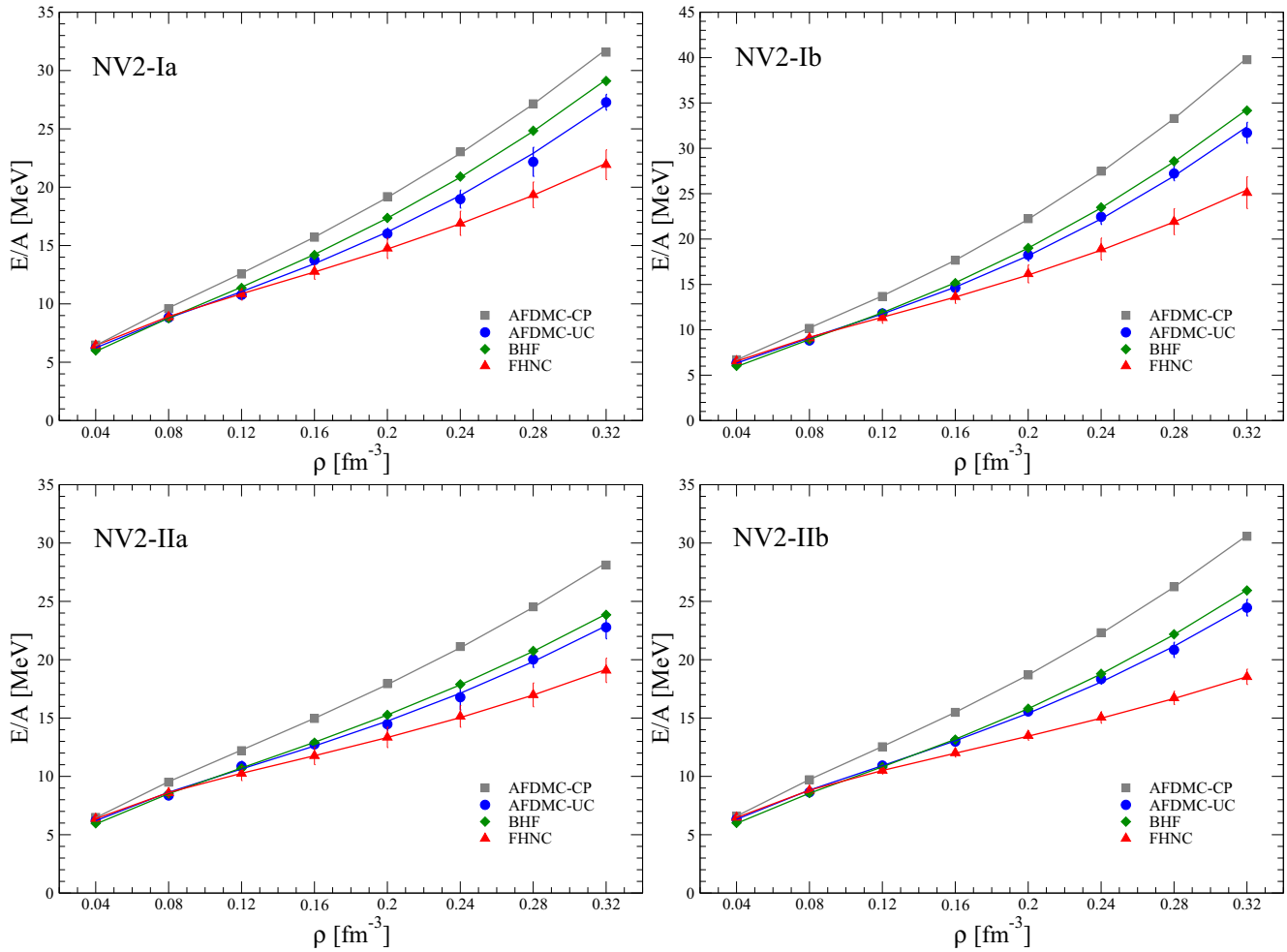

FIG. 7. Same as Fig. 6 for the NV2-Ia (upper left panel), NV2-Ib (upper right panel), NV2-IIa (lower left panel), and NV2-IIb (lower right panel) potentials.

This might once more be ascribed to the three-body truncation in the cluster expansion of the spin-orbit correlations.

In the lower panel of Fig. 6, we also compare our BHF results for the AV18 interaction with those reported in Ref. [67]. We do not display the BHF curve, as it is almost coincident with ours. At $\rho = 0.3$ fm^{-3}, we obtain an energy per particle of 26.0 MeV, to be compared to the 25.4 MeV of Ref. [67]. The small difference can be attributed to the different number of partial waves: $J_{\max} = 11$ in our case and $J_{\max} = 8$ in Ref. [67]. In fact, using $J_{\max} = 8$ we also get 25.6 MeV. The results of the energy per particle up to the three-hole line diagrams contribution of the BBG hole-line expansion, as taken from Ref. [67] are represented by the purple triangles labeled as BBG$_3$. As shown in Refs. [92,93] and as stressed in Sec. III A of the present work, comparing the BBG$_3$ and the BHF predictions numerically demonstrates the fast convergence of the hole-line expansion when the continuous choice for the auxiliary single particle potential $U(k)$ of Eq. (9) is used. Finally, in the same figure, we also plot the self-consistent Green's function (SCGF) results reported in Ref. [67].

The differences among the many-body methods discussed above are reflected in the contribution of the spin-orbit terms to the energy per particle. AFDMC-CP calculations clearly underestimate $\langle v_{\rm LS}\rangle$, as it turns out to be much smaller than 1 MeV per particle for both the AV8′ and AV18 potentials—see Table I. The unconstrained propagation enhances the spin-orbit contribution. Nevertheless, the AFDMC-UC values remain well below the BHF and FHNC/SOC results. The Hellman-Feynman procedure brings about sizable uncertainties in the AFDMC-UC estimates, of about 1.2 MeV per particle for all the potentials that we consider. Applying the error propagation formula to Eq. (48), the individual errors on $E_{\pm\epsilon}$ are enhanced by a factor $\sim 1/\epsilon$, and we take $\epsilon = 0.1$. In addition, a stronger spin-orbit term, even by only 10%, brings about significantly larger statistical errors in the unconstrained propagation. However, the AFDMC-CP estimates for $\langle v_{\rm LS}\rangle$ do not suffer from these additional statistical fluctuations. To control this AFDMC-UC error, when computing $\langle v_{\rm LS}\rangle$ we accumulate more statistics (more Monte Carlo configurations) than in standard calculations of the energy per particle. As a consequence, the uncertainties on the AFDMC-CP estimates for the spin-orbit term are not $\simeq 1/\epsilon$ larger than those of the energy per particle.

Figure 7 displays the energy per particle of the NV2-Ia, NV2-Ib, NV2-IIa, and NV2-IIb potentials as computed within

TABLE II. Same as Table I for the NV2-Ia, NV2-Ib, NV2-IIa, and NV2-IIb potentials.

	BHF	FHNC/SOC	AFDMC-CP	AFDMC-UC
		E/A [MeV]		
NV2-Ia	14.19	12.77 ± 0.67	15.71 ± 0.02	13.75 ± 0.34
NV2-Ib	15.14	13.64 ± 0.74	17.67 ± 0.02	14.67 ± 0.48
NV2-IIa	12.89	11.77 ± 0.76	14.97 ± 0.02	12.74 ± 0.32
NV2-IIb	13.15	12.01 ± 0.36	15.49 ± 0.02	12.94 ± 0.27
				$\langle v_{\rm LS} \rangle$ [MeV]
NV2-Ia	−5.32	−7.88	-0.37 ± 0.03	-5.0 ± 1.1
NV2-Ib	−8.88	−9.95	-0.50 ± 0.03	-6.2 ± 1.3
NV2-IIa	−6.23	−7.78	-0.39 ± 0.03	-4.6 ± 1.2
NV2-IIb	−6.56	−7.48	-0.50 ± 0.03	-4.9 ± 1.1

the different many-body methods and their polynomial fit using the expression of Eq. (47). The picture that emerges is fully consistent with the one already discussed for the AV8′ and AV18 interactions. Looking at the values listed in Table II, it is apparent that AFDMC-CP calculations suffer from a substantial systematic error: releasing the constraint in the imaginary-time propagation lowers the energy per particle by at least ∼2 MeV per nucleon, improving the agreement with BHF and FHNC/SOC calculations. Consistently with the AV8′ and AV18 potentials, the AFDMC-UC values for $\langle v_{\rm LS} \rangle$ are smaller than those obtained within the BHF and FHNC/SOC methods. The bias of the AFDMC-CP results increases with the density: releasing the constraint in the imaginary-time propagation lowers the energy per particle by as much as ∼8 MeV at $\rho = 2\rho_0$ for the NV2-Ib model. The good agreement between BHF and AFDMC-UC is to a large extent confirmed, as the discrepancies between the two methods are smaller than ∼2.5 MeV for all the densities and potentials we analyzed. Once again, for densities larger than ρ_0, FHNC/SOC calculations yield considerably lower energies than BHF and AFDMC-UC. Comparing Tables I and II, we see that for the Argonne interactions, the $\langle v_{\rm LS} \rangle$ is smaller in the FHNC/SOC calculations compared to BHF, while the opposite is true for the Norfolk potentials. Also, the error bar on the total energy attached to the FHNC/SOC calculations is much larger for all the Norfolk interactions.

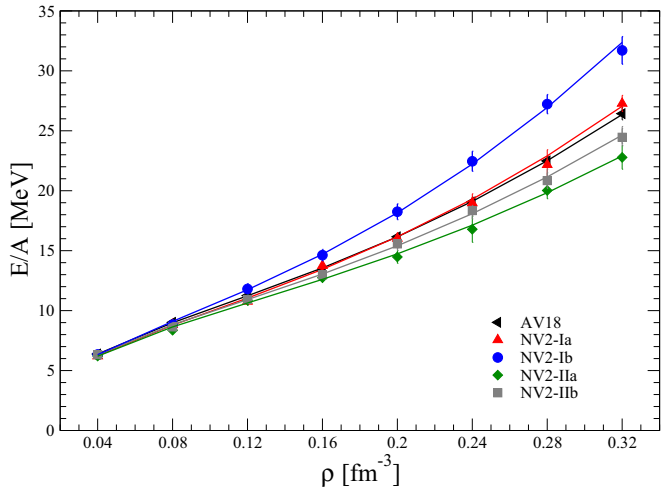

FIG. 8. AFDMC-UC energy per particle of PNM as a function of density for the AV18 (black triangles), NV2-Ia (red triangles), NV2-Ib (solid blue points), NV2-IIa (green diamonds), and NV2-IIb (grey squares) potentials.

TABLE III. Best-fit parameters from Eq. (47) for the AFDMC-UC energy per particle displayed in Fig 8. All values are in MeV.

	$a_{2/3}$	a_1	a_2
AV18	26.99 ± 0.24	-18.61 ± 0.38	5.18 ± 0.12
NV2-Ia	26.65 ± 1.09	-18.79 ± 1.59	5.58 ± 0.44
NV2-Ib	27.08 ± 0.86	-19.46 ± 1.34	7.07 ± 0.40
NV2-IIa	26.17 ± 0.86	-17.81 ± 1.37	4.24 ± 0.42
NV2-IIb	27.01 ± 0.60	-18.80 ± 0.95	4.84 ± 0.30

By taking the AFDMC-UC results as our reference, in Fig. 8 we display the EoS obtained using the AV18 and the NV2 potentials. The parameters of the polynomial fit of Eq. (47) along with their uncertainties are reported in Table III. The latter are determined assuming that the energy per particle and their errors are statistically independent and have a Gaussian distribution. Comparing the EoS obtained using the AV18 and the NV2 potentials we observe that, with the exception of the NV2-Ib case, the maximum spread among the curves is well within 5 MeV per particle up to $\rho = 2\rho_0$. In fact, for densities smaller than nuclear saturation, the differences are always below ∼1 MeV per particle.

The NV2 energy results are ordered from most repulsive to least repulsive as Ib > Ia > IIb > IIa. This is the same order observed in GFMC calculations of the energy of ^{4}He in Ref. [65], where they give −22.89, −25.13, −25.21, and −25.71 MeV, respectively, with Ib the least bound (by a wide margin) and IIa the most bound. As noted there, the spread in characteristics due to variations in the cut-off parameters is noticeably reduced by fitting the *NN* data to higher laboratory energy, i.e., models IIa and IIb are closer together than Ia and Ib. Also, the "softer" the potential, the more attractive it is, i.e., Ia is below Ib and IIa is below IIb. Finally, the fit to higher energy has produced somewhat more attraction, i.e., both models II are more attractive than models I. Comparing the phase shifts in Fig. 2, it would appear that NV2-IIb has the best reproduction of data and it is fairly close to AV18.

It is also interesting to compare the uncertainties on the EoS arising from the many-body method versus those associated to the nucleon-nucleon interaction. At saturation density, the AFDMC-UC, BHF and FHNC/SOC calculations for all the potentials we consider are within 1.5 MeV per particle. The maximum difference among the AFDMC-UC values for the energy per particle obtained from different interactions is slightly larger, of about 1.9 MeV. At twice saturation density, the spread among the many-body methods is 9.7 MeV per particle, to be compared to the 8.7 MeV associated with the nuclear potentials (less if model NV2-Ib is excluded).

V. CONCLUSIONS

We have carried out benchmark calculations of the energy per particle of pure neutron matter as a function of the

baryon density, employing two distinct families of coordinate-space nucleon-nucleon potentials in three independent nuclear many-body methods: AFDMC, FHNC/SOC, and BHF. As for the nuclear Hamiltonians, we have considered the phenomenological Argonne AV6′, AV8′ [63], and AV18 two-body interactions [62], and the set of Norfolk χEFT NV2 potentials [64,65], which explicitly includes Δ-isobar intermediate states. With the exception of AV6′, these potentials are characterized by relatively strong spin-orbit components, needed to reproduce the *NN* phase shifts in *P* and higher odd partial waves.

Our pure neutron matter AFDMC calculations are performed using the "plus and minus" importance-sampling algorithm, introduced in Ref. [68] to treat atomic nuclei and isospin-symmetric and asymmetric nuclear matter. However, previous application of the AFDMC method to purely-neutron systems used a different importance sampling for both the spacial coordinates and the auxiliary fields. Extending the analysis of Refs. [111,117], we have investigated the systematic error of the AFDMC method arising from constraining the imaginary-time propagation to alleviate the fermion-sign problem. We have performed unconstrained imaginary-time propagations up to 0.004 MeV^{-1}, extrapolating the asymptotic value for the energy per particle using a single-exponential fit. By computing the covariance matrix of the data to account for the correlations among the AFDMC samples, we are able to estimate the uncertainty of the asymptotic energy by varying the χ^2 contour of the fit. The FHNC/SOC method has been improved by systematically including sets of elementary diagrams, at and beyond the FHNC/4 approximation, through the use of three-point superbonds in the diagrammatic expansion. However, the most relevant numerical difference with the FHNC/SOC results reported in Ref. [67] is the inclusion of spin-orbit correlations.

When the AV6′ interaction is employed, AFDMC, FHNC/SOC, and BHF yield similar energies per particle, the maximum difference among the methods remaining smaller than 5 MeV per particle up to $\rho = 2\rho_0$. The excellent agreement between AFDMC and FHNC/SOC calculations has to be ascribed to both the improved sampling in the AFDMC method and to the inclusion of the elementary diagrams in FHNC/SOC. Releasing the constraint on the imaginary-time propagation does not bring about appreciable difference with respect to the AFDMC-CP results. Notice that the moderate differences between the BHF EoS and those for the AFDMC and FHNC/SOC methods are partially reduced when the contribution of the three-hole line diagrams is added to the BHF results (BBG_3). For example, at $\rho = 2\rho_0$ one has $(E/A)_{\mathrm{BBG}_3} = 28.7\,\mathrm{MeV}$ [67] which is in better agreement with the AFDMC and FHNC/SOC results. Clearly we checked that for the AV6′ potential our BHF results overlap with those of Ref. [67].

However, when spin-orbit terms are present in the nuclear interaction, we find that performing unconstrained propagations is crucial to reliably compute the equation of state of neutron matter. Simple constrained propagation significantly overestimates the energy per particle, with the bias increasing with the density. For instance, when the AV18 potential is used, the difference between AFDMC-CP and AFDMC-UC calculations can be as large as $\sim$3 MeV at $\rho = \rho_0$ and $\sim$7 MeV at $\rho = 2\rho_0$. Similar trends are also found for the AV8′ potential and all NV2 interactions and we can reasonably expect that analogous systematic errors affect the AFDMC calculations of neutron-matter properties carried out with local N2LO χEFT Hamiltonians [43,70,71,74,101].

The AFDMC-UC predictions are in good agreement with those of the BHF approach. For both AV18 and the NV2 potentials, the discrepancies between the two methods remain well within 3 MeV per particle, with the AFDMC-UC method always providing less repulsion than the BHF. This highly non trivial outcome of our comparison has been enabled by the possibility of performing unconstrained propagations in AFDMC. As a matter of fact, the AFDMC-CP equations of state are sizably above both BHF and AFDMC-UC ones. The FHNC/SOC energies per particle are consistently below those computed within the other two many-body methods, particularly for densities larger than ρ_0. This is likely to be ascribed to the somewhat oversimplified treatment of spin-orbit correlations, whose contributions are exactly treated only at the two-body cluster level. Only a limited number of three-body terms in the cluster expansion are kept, as in Ref. [35]. An alternate selection of three-body terms is followed in Ref. [36]. We plan to compare with this latter choice in the future to see if there is better agreement with the new AFDMC and BHF results. Limiting our analysis to $\rho \leqslant \rho_0$, where higher-order terms in the cluster expansion are smaller, FHNC/SOC and AFDMC-UC agree within 1 MeV per particle, while the difference between AFDMC-CP and FHNC/SOC turns out to be significantly larger.

The AV18 potential fits *NN* scattering data with $\chi^2 \sim 1$ in the energy range $0 \leqslant E_{\mathrm{lab}} \leqslant 350\,\mathrm{MeV}$, while NV2 potentials are constrained up to lower energies: $0 \leqslant E_{\mathrm{lab}} \leqslant 125$ and $0 \leqslant E_{\mathrm{lab}} \leqslant 200\,\mathrm{MeV}$ for class I and class II, respectively. Hence, the AV18, NV2-IIa, and NV2-IIb reproduce the experimental proton-neutron scattering phase shifts in the $^1\mathrm{S}_0$, $^3\mathrm{P}_0$, $^3\mathrm{P}_1$, $^3\mathrm{P}_2$, ϵ_2, and $^1\mathrm{D}_2$ partial waves to higher energies than NV2-Ia and NV2-Ib. Since in highly degenerate matter neutron-neutron collisions mostly take place in the vicinity of the Fermi surface, one can reasonably expect that potential models capable of reproducing *NN* scattering to higher E_{lab} will more reliably predict the EoS at larger densities. Our AFDMC-UC calculations indicate that this is indeed the case. The maximum spread among the energies per particle obtained using the AV18, NV2-IIa, and NV2-IIb potentials is well within 4 MeV per particle up to twice nuclear saturation density. However, including NV2-Ia and NV2-Ib, the spread among the models can be as large as $\sim$9 MeV per particle.

This work extends the benchmark calculations carried out in the literature [67,121,122] and it is not aimed at obtaining a realistic description of the neutron matter EoS, for which three-body forces are required. Two classes of χEFT three-nucleon interactions consistent with the Δ-full *NN* potentials employed in this work have been derived and successfully applied to describe the spectrum of light nuclei [76] and the β-decay of $^3\mathrm{H}$ [77]. Once implemented in our many-body methods, we will compute the EoS and check their compatibility with astrophysical constraints, gauging potential

regulator artifacts [74,120,123] and the convergence of the chiral expansion.

ACKNOWLEDGMENTS

We thank J. Carlson, D. Lonardoni, L. Riz, and I. Tews for valuable discussions. This research is supported by the US Department of Energy, Office of Science, Office of Nuclear Physics, under Contract No. DE-AC02-06CH11357 (A.L. and R.B.W.) and under FRIB Theory Alliance Award No. DE-SC0013617 (M.P.) as well as the NUCLEI SciDAC program. Under an award of computer time provided by the INCITE program, this research used resources of the Argonne Leadership Computing Facility at Argonne National Laboratory, which is supported by the Office of Science of the US Department of Energy under Contract No. DE-AC02-06CH11357. Numerical calculations have been made possible also through a CINECA-INFN agreement, providing access to resources on MARCONI at CINECA, and through the Argonne Laboratory Computing Resource Center.

[1] S. Weinberg, Phys. Lett. B **251**, 288 (1990).
[2] S. Weinberg, Nucl. Phys. B **363**, 3 (1991).
[3] E. Epelbaum, H.-W. Hammer, and U.-G. Meissner, Rev. Mod. Phys. **81**, 1773 (2009).
[4] R. Machleidt and D. R. Entem, Phys. Rept. **503**, 1 (2011).
[5] P. Reinert, H. Krebs, and E. Epelbaum, Eur. Phys. J. A **54**, 86 (2018).
[6] D. R. Entem, R. Machleidt, and Y. Nosyk, Phys. Rev. C **96**, 024004 (2017).
[7] S. Pastore, L. Girlanda, R. Schiavilla, M. Viviani, and R. B. Wiringa, Phys. Rev. C **80**, 034004 (2009).
[8] S. Kolling, E. Epelbaum, H. Krebs, and U. G. Meissner, Phys. Rev. C **80**, 045502 (2009).
[9] S. Pastore, L. Girlanda, R. Schiavilla, and M. Viviani, Phys. Rev. C **84**, 024001 (2011).
[10] S. Kolling, E. Epelbaum, H. Krebs, and U. G. Meissner, Phys. Rev. C **84**, 054008 (2011).
[11] A. Baroni, L. Girlanda, S. Pastore, R. Schiavilla, and M. Viviani, Phys. Rev. C **93**, 015501 (2016) [Erratum: Phys. Rev. C **95**, 059901 (2017)].
[12] H. Krebs, E. Epelbaum, and U. G. Meißner, Ann. Phys. **378**, 317 (2017).
[13] A. Baroni, L. Girlanda, A. Kievsky, L. E. Marcucci, R. Schiavilla, and M. Viviani, Phys. Rev. C **94**, 024003 (2016) [Erratum: Phys. Rev. C **95**, 059902 (2017)].
[14] H. J. Schulze, J. Cugnon, A. Lejeune, M. Baldo, and U. Lombardo, Phys. Rev. C **52**, 2785 (1995).
[15] M. Baldo and G. F. Burgio, Rep. Prog. Phys. **75**, 026301 (2012).
[16] A. Carbone, A. Cipollone, C. Barbieri, A. Rios, and A. Polls, Phys. Rev. C **88**, 054326 (2013).
[17] B. R. Barrett, P. Navratil, and J. P. Vary, Prog. Part. Nucl. Phys. **69**, 131 (2013).
[18] G. Hagen, T. Papenbrock, M. Hjorth-Jensen, and D. J. Dean, Rept. Prog. Phys. **77**, 096302 (2014).
[19] J. Carlson, S. Gandolfi, F. Pederiva, S. C. Pieper, R. Schiavilla, K. E. Schmidt, and R. B. Wiringa, Rev. Mod. Phys. **87**, 1067 (2015).
[20] H. Hergert, S. K. Bogner, T. D. Morris, A. Schwenk, and K. Tsukiyama, Phys. Rept. **621**, 165 (2016).
[21] B. P. Abbott *et al.* (LIGO Scientific, Virgo, Fermi GBM, INTEGRAL, IceCube, AstroSat Cadmium Zinc Telluride Imager Team, IPN, Insight-Hxmt, ANTARES, Swift, AGILE Team, 1M2H Team, Dark Energy Camera GW-EM, DES, DLT40, GRAWITA, Fermi-LAT, ATCA, ASKAP, Las Cumbres Observatory Group, OzGrav, DWF (Deeper Wider Faster Program), AST3, CAASTRO, VINROUGE, MASTER, J-GEM, GROWTH, JAGWAR, CaltechNRAO, TTU-NRAO, NuSTAR, Pan-STARRS, MAXI Team, TZAC Consortium, KU, Nordic Optical Telescope, ePESSTO, GROND, Texas Tech University, SALT Group, TOROS, BOOTES, MWA, CALET, IKI-GW Follow-up, H.E.S.S., LOFAR, LWA, HAWC, Pierre Auger, ALMA, Euro VLBI Team, Pi of Sky, Chandra Team at McGill University, DFN, ATLAS Telescopes, High Time Resolution Universe Survey, RIMAS, RATIR, SKA South Africa/MeerKAT), Astrophys. J. **848**, L12 (2017).
[22] LIGO Scientific Collaboration, http://www.ligo.org.
[23] VIRGO Collaboration, http://www.virgo-gw.eu.
[24] B. P. Abbott *et al.* (LIGO Scientific, Virgo), Phys. Rev. Lett. **119**, 161101 (2017).
[25] B. P. Abbott *et al.* (LIGO Scientific, Virgo), Phys. Rev. X **9**, 011001 (2019).
[26] I. Tews, J. Margueron, and S. Reddy, Phys. Rev. C **98**, 045804 (2018).
[27] M. Fasano, T. Abdelsalhin, A. Maselli, and V. Ferrari, Phys. Rev. Lett. **123**, 141101 (2019).
[28] P. Demorest, T. Pennucci, S. Ransom, M. Roberts, and J. Hessels, Nature **467**, 1081 (2010).
[29] R. S. Lynch *et al.*, Astrophys. J. **763**, 81 (2013).
[30] J. Antoniadis *et al.*, Science **340**, 1233232 (2013).
[31] Z. Arzoumanian *et al.* (NANOGrav), Astrophys. J. Suppl. **235**, 37 (2018).
[32] H. T. Cromartie *et al.*, Nat. Astronomy **4**, 72 (2020).
[33] M. Prakash, I. Bombaci, M. Prakash, P. J. Ellis, J. M. Lattimer, and R. Knorren, Phys. Rept. **280**, 1 (1997).
[34] B. Friedman and V. R. Pandharipande, Nucl. Phys. A **361**, 502 (1981).
[35] R. B. Wiringa, V. Fiks, and A. Fabrocini, Phys. Rev. C **38**, 1010 (1988).
[36] A. Akmal, V. R. Pandharipande, and D. G. Ravenhall, Phys. Rev. C **58**, 1804 (1998).
[37] M. Baldo, I. Bombaci, and G. F. Burgio, Astron. Astrophys. **328**, 274 (1997).
[38] W. Zuo, I. Bombaci, and U. Lombardo, Phys. Rev. C **60**, 024605 (1999).
[39] G. Baardsen, A. Ekström, G. Hagen, and M. Hjorth-Jensen, Phys. Rev. C **88**, 054312 (2013).
[40] G. Hagen, T. Papenbrock, A. Ekström, K. A. Wendt, G. Baardsen, S. Gandolfi, M. Hjorth-Jensen, and C. J. Horowitz, Phys. Rev. C **89**, 014319 (2014).

[41] A. Roggero, A. Mukherjee, and F. Pederiva, Phys. Rev. Lett. **112**, 221103 (2014).
[42] A. Carbone, A. Rios, and A. Polls, Phys. Rev. C **90**, 054322 (2014).
[43] J. E. Lynn, I. Tews, J. Carlson, S. Gandolfi, A. Gezerlis, K. E. Schmidt, and A. Schwenk, Phys. Rev. Lett. **116**, 062501 (2016).
[44] I. Bombaci and D. Logoteta, Astron. Astrophys. **609**, A128 (2018).
[45] N. K. Glendenning, Astrophys. J. **293**, 470 (1985).
[46] I. Vidana, D. Logoteta, C. Providencia, A. Polls, and I. Bombaci, Europhys. Lett. **94**, 11002 (2011).
[47] D. Lonardoni, A. Lovato, S. Gandolfi, and F. Pederiva, Phys. Rev. Lett. **114**, 092301 (2015).
[48] D. Chatterjee and I. Vidana, Eur. Phys. J. A **52**, 29 (2016).
[49] J. Haidenbauer, U. G. Meißner, N. Kaiser, and W. Weise, Eur. Phys. J. A **53**, 121 (2017).
[50] I. F. Ranea-Sandoval, S. Han, M. G. Orsaria, G. A. Contrera, F. Weber, and M. G. Alford, Phys. Rev. C **93**, 045812 (2016).
[51] M. G. Alford, G. F. Burgio, S. Han, G. Taranto, and D. Zappalá, Phys. Rev. D **92**, 083002 (2015).
[52] M. Mariani, M. Orsaria, and H. Vucetich, Astron. Astrophys. **601**, A21 (2017).
[53] I. Bombaci, D. Logoteta, I. Vidaña, and C. Providência, Eur. Phys. J. A **52**, 58 (2016).
[54] V. R. Pandharipande, C. J. Pethick, and V. Thorsson, Phys. Rev. Lett. **75**, 4567 (1995).
[55] N. K. Glendenning and J. Schaffner-Bielich, Phys. Rev. C **60**, 025803 (1999).
[56] A. Mukherjee, Phys. Rev. C **79**, 045811 (2009).
[57] E. Epelbaum, H. Krebs, and U. G. Meißner, Eur. Phys. J. A **51**, 53 (2015).
[58] B. D. Day, Rev. Mod. Phys. **39**, 719 (1967).
[59] S. Fantoni and S. Rosati, Nuovo Cimento A **25**, 593 (1975).
[60] V. R. Pandharipande and R. B. Wiringa, Rev. Mod. Phys. **51**, 821 (1979).
[61] K. E. Schmidt and S. Fantoni, Phys. Lett. B **446**, 99 (1999).
[62] R. B. Wiringa, V. G. J. Stoks, and R. Schiavilla, Phys. Rev. C **51**, 38 (1995).
[63] R. B. Wiringa and S. C. Pieper, Phys. Rev. Lett. **89**, 182501 (2002).
[64] M. Piarulli, L. Girlanda, R. Schiavilla, R. N. Pérez, J. E. Amaro, and E. R. Arriola, Phys. Rev. C **91**, 024003 (2015).
[65] M. Piarulli, L. Girlanda, R. Schiavilla, A. Kievsky, A. Lovato, L. E. Marcucci, S. C. Pieper, M. Viviani, and R. B. Wiringa, Phys. Rev. C **94**, 054007 (2016).
[66] J. E. Lynn and K. E. Schmidt, Phys. Rev. C **86**, 014324 (2012).
[67] M. Baldo, A. Polls, A. Rios, H. J. Schulze, and I. Vidana, Phys. Rev. C **86**, 064001 (2012).
[68] S. Gandolfi, A. Lovato, J. Carlson, and K. E. Schmidt, Phys. Rev. C **90**, 061306 (2014).
[69] D. Lonardoni, S. Gandolfi, J. E. Lynn, C. Petrie, J. Carlson, K. E. Schmidt, and A. Schwenk, Phys. Rev. C **97**, 044318 (2018).
[70] A. Gezerlis, I. Tews, E. Epelbaum, S. Gandolfi, K. Hebeler, A. Nogga, and A. Schwenk, Phys. Rev. Lett. **111**, 032501 (2013).
[71] A. Gezerlis, I. Tews, E. Epelbaum, M. Freunek, S. Gandolfi, K. Hebeler, A. Nogga, and A. Schwenk, Phys. Rev. C **90**, 054323 (2014).
[72] O. Benhar, arXiv:1903.11353.
[73] J. E. Lynn, J. Carlson, E. Epelbaum, S. Gandolfi, A. Gezerlis, and A. Schwenk, Phys. Rev. Lett. **113**, 192501 (2014).
[74] I. Tews, S. Gandolfi, A. Gezerlis, and A. Schwenk, Phys. Rev. C **93**, 024305 (2016).
[75] J. E. Lynn, I. Tews, J. Carlson, S. Gandolfi, A. Gezerlis, K. E. Schmidt, and A. Schwenk, Phys. Rev. C **96**, 054007 (2017).
[76] M. Piarulli *et al.*, Phys. Rev. Lett. **120**, 052503 (2018).
[77] A. Baroni *et al.*, Phys. Rev. C **98**, 044003 (2018).
[78] R. N. Pérez, J. E. Amaro, and E. R. Arriola, Phys. Rev. C **88**, 064002 (2013) [Erratum: Phys. Rev. C **91**, 029901 (2015)].
[79] B. S. Pudliner, V. R. Pandharipande, J. Carlson, S. C. Pieper, and R. B. Wiringa, Phys. Rev. C **56**, 1720 (1997).
[80] R. L. Workman, W. J. Briscoe, and I. I. Strakovsky, Phys. Rev. C **94**, 065203 (2016).
[81] S. K. Bogner, R. J. Furnstahl, and A. Schwenk, Prog. Part. Nucl. Phys. **65**, 94 (2010).
[82] J. Goldstone, Proc. R. Soc. London A **239**, 267 (1957).
[83] K. A. Brueckner, C. A. Levinson, and H. M. Mahmoud, Phys. Rev. **95**, 217 (1954).
[84] K. A. Brueckner, Phys. Rev. **96**, 508 (1954).
[85] H. A. Bethe and J. Goldstone, Proc. R. Soc. London A **238**, 551 (1957).
[86] H. A. Bethe, B. H. Brandow, and A. G. Petschek, Phys. Rev. **129**, 225 (1963).
[87] J. Hufner and C. Mahaux, Ann. Phys. **73**, 525 (1972).
[88] J. P. Jeukenne, A. Lejeune, and C. Mahaux, Phys. Rep. **25**, 83 (1976).
[89] P. Grangé, J. Cugnon, and A. Lejeune, Nucl. Phys. A **473**, 365 (1987).
[90] M. Baldo, I. Bombaci, G. Giansiracusa, U. Lombardo, C. Mahaux, and R. Sartor, Phys. Rev. C **41**, 1748 (1990).
[91] M. Baldo, I. Bombaci, L. S. Ferreira, G. Giansiracusa, and U. Lombardo, Phys. Rev. C **43**, 2605 (1991).
[92] H. Q. Song, M. Baldo, G. Giansiracusa, and U. Lombardo, Phys. Lett. B **411**, 237 (1997).
[93] M. Baldo, G. Giansiracusa, U. Lombardo, and H. Q. Song, Phys. Lett. B **473**, 1 (2000).
[94] J.-J. Lu, Z.-H. Li, C.-Y. Chen, M. Baldo, and H. J. Schulze, Phys. Rev. C **98**, 064322 (2018).
[95] R. Jastrow, Phys. Rev. **98**, 1479 (1955).
[96] J. M. J. van Leeuwen, J. Groeneveld, and J. de Boer, Physica (Utrecht) **25**, 792 (1959).
[97] V. R. Pandharipande and H. A. Bethe, Phys. Rev. C **7**, 1312 (1973).
[98] H. W. Jackson and E. Feenberg, Rev. Mod. Phys. **34**, 686 (1962).
[99] J. G. Zabolitzky, Phys. Rev. A **16**, 1258 (1977).
[100] Q. N. Usmani, B. Friedman, and V. R. Pandharipande, Phys. Rev. B **25**, 4502 (1982).
[101] I. Tews, J. Carlson, S. Gandolfi, and S. Reddy, Astrophys. J. **860**, 149 (2018).
[102] S. Fantoni, S. Gandolfi, A. Yu. Illarionov, K. E. Schmidt, and F. Pederiva, in *Sixth International Conference on Perspectives in Hadronic Physics*, edited by S. Boffi, C. C. d. Atti, M. Giannini, and D. Treleani, AIP Conf. Proc. No. 1056 (AIP, New York, 2008), p. 233.
[103] S. Gandolfi, A. Yu. Illarionov, K. E. Schmidt, F. Pederiva, and S. Fantoni, Phys. Rev. C **79**, 054005 (2009).
[104] A. Sarsa, S. Fantoni, K. E. Schmidt, and F. Pederiva, Phys. Rev. C **68**, 024308 (2003).

[105] D. Lonardoni, J. Carlson, S. Gandolfi, J. E. Lynn, K. E. Schmidt, A. Schwenk, and X. B. Wang, Phys. Rev. Lett. **120**, 122502 (2018).
[106] S. Sorella, Phys. Rev. B **71**, 241103 (2005).
[107] J. Toulouse and C. J. Umrigar, J. Chem. Phys. **126**, 084102 (2007).
[108] S. Zhang and H. Krakauer, Phys. Rev. Lett. **90**, 136401 (2003).
[109] S. Zhang, J. Carlson, and J. E. Gubernatis, Phys. Rev. B **55**, 7464 (1997).
[110] R. B. Wiringa, S. C. Pieper, J. Carlson, and V. R. Pandharipande, Phys. Rev. C **62**, 014001 (2000).
[111] F. Pederiva, A. Sarsa, K. E. Schmidt, and S. Fantoni, Nucl. Phys. A **742**, 255 (2004).
[112] B. Yoon, Y.-C. Jang, C. Jung, and W. Lee, J. Korean Phys. Soc. **63**, 145 (2013).
[113] W. H. Press, S. A. Teukolsky, W. T. Vetterling, and B. P. Flannery, *Numerical Recipes in FORTRAN: The Art of Scientific Computing*, 2nd ed. (Cambridge University Press, New York, NY, 1993).
[114] D. Lonardoni, S. Gandolfi, X. B. Wang, and J. Carlson, Phys. Rev. C **98**, 014322 (2018).
[115] A. Lovato, O. Benhar, S. Fantoni, A. Yu. Illarionov, and K. E. Schmidt, Phys. Rev. C **83**, 054003 (2011).
[116] L. Brualla, S. Fantoni, A. Sarsa, K. E. Schmidt, and S. A. Vitiello, Phys. Rev. C **67**, 065806 (2003).
[117] J. Carlson, J. Morales, Jr., V. R. Pandharipande, and D. G. Ravenhall, Phys. Rev. C **68**, 025802 (2003).
[118] S. Gandolfi, J. Carlson, S. Reddy, A. W. Steiner, and R. B. Wiringa, Eur. Phys. J. A **50**, 10 (2014).
[119] R. B. Wiringa and S. C. Pieper, Evolution of Nuclear Spectra with Nuclear Forces, https://www.phy.anl.gov/theory/fewbody/avxp_results.html (dated July 15, 2002).
[120] A. Lovato, O. Benhar, S. Fantoni, and K. E. Schmidt, Phys. Rev. C **85**, 024003 (2012).
[121] M. Baldo and C. Maieron, Phys. Rev. C **69**, 014301 (2004).
[122] I. Bombaci, A. Fabrocini, A. Polls, and I. Vidana, Phys. Lett. B **609**, 232 (2005).
[123] L. Huth, I. Tews, J. E. Lynn, and A. Schwenk, Phys. Rev. C **96**, 054003 (2017).